

1 Revision 4

2 11,049 words

3
4 **Geochemical characteristics of mineral inclusions in the Luobusa**
5 **chromitite (Southern Tibet): Implications for an intricate geological setting**
6

7
8 Fahui Xiong^{1,2,*}, Basem Zoheir^{3,4,*}, Xiangzhen Xu¹, Guolin Guo⁵, Matthias Frische⁶,
9 Jingsui Yang^{1,2}

10
11
12 *¹Center for Advanced Research on the Mantle (CARMA), Key Laboratory of Deep-*
13 *Earth Dynamics of Ministry of Land and Resources, SinoProbe Laboratory, Institute*
14 *of Geology, Chinese Academy of Geological Sciences, Beijing 100037, China*

15 *²Research Center of Continental Dynamics, College of Earth Science and*
16 *Engineering, Shandong University of Science and Technology, Qingdao, China*

17 *³Department of Geology, Faculty of Science, Benha University, 13518 Benha, Egypt*

18 *⁴Institute of Geosciences, University of Kiel, Ludewig-Meyn Str. 10, 24118 Kiel,*
19 *Germany*

20 *⁵School of earth sciences, East China University of Technology, Nanchang, 330013,*
21 *Jiangxi, China*

22 *⁶GEOMAR Helmholtz Centre for Ocean Research Kiel, Wischhofstr. 1-3, 24148 Kiel,*
23 *Germany*

24
25
26
27 ** Corresponding authors: Fahui Xiong (xiongfahui@126.com), Basem Zoheir*
28 *(basem.zoheir@gmail.com)*

32

ABSTRACT

33 The Luobusa chromitite and ophiolite present a captivating geological feature
34 marked by peculiar mineralogical and geochemical characteristics. Abundant
35 platinum-group minerals (PGM), base-metal sulfides (BMS), and PGE-sulfides and
36 alloys in the chromitite unveil a multi-stage genesis, encompassing partial mantle
37 melting, melt-rock interactions, and dynamic shifts in oxygen and sulfur fugacity
38 (fO_2 , fS_2). This study explores the geochemical signatures and PGE patterns of
39 these mineral inclusions to elucidate the evolutionary process of the Luobusa
40 ophiolite, tracing its transition from a sub-ridge environment to a sub-arc setting.
41 The variable Σ PGE values (40 - 334 ppb) in chromitite, coupled with notably lower
42 Σ PGE values (10 - 63 ppb) in dunite imply extensive melt fractionation and melt-
43 rock interactions. Coexisting well-crystalline Os-Ir alloys alongside interstitial
44 BMS likely reflect low fS_2 and high temperatures during the early formational
45 stages, whereas abundant anhedral sulfarsenide and pyrite inclusions in chromite
46 point to lower temperatures and higher fS_2 during the late stages. The trace
47 element composition of pyrite inclusions resonates with the characteristics of
48 mid-ocean ridge (MOR) and oceanic island rocks, manifesting interplay of diverse
49 magmatic sources during the evolution of the Luobusa ophiolite.

50

51 **Keywords:** *Luobusa ophiolite, SW Tibet, chromitite, PGM and BMS inclusions,*
52 *genetic model.*

53

54 INTRODUCTION

55 Podiform chromitites commonly occur as lenticular or ellipsoidal bodies
56 associated with ophiolitic nappes (Arai 1997 and references therein). Despite
57 ongoing scientific research and data accumulation, the origin of these chromitites
58 has been the subject of continued debate (e.g., He et al. 2021; Yang et al. 2021; Yao
59 et al. 2023). Early studies proposed that podiform chromitites result from

60 differential gravitational separation of mantle-derived magmas (Dickey 1975;
61 Mondal and Mathez 2007; Maier et al. 2013). Other hypotheses suggest reactions
62 between basaltic melts and mantle peridotites (e.g., Zhou et al. 1994; Arai and
63 Miura 2016) or crystallization of chromite from immiscible melts (Matveev and
64 Ballhaus 2002; Su et al. 2020, 2021a, b). High-Al chromitites are believed to form
65 in mid-ocean ridge environments (MOR) with MORB melt, while high-Cr
66 chromitites are typically associated with supra-subduction zone (SSZ) processes
67 by melt reaction with boninitic melt (e.g., Zhou et al. 2005; Arai and Miura 2016).
68 The coexistence of high-Al and high-Cr ores may reflect the long-term evolution of
69 the associated ophiolitic complexes (Xiong et al. 2017, 2018; Ullah et al. 2020,
70 2022; Zhang et al. 2023).

71 Integration of the geochemical properties of ophiolitic chromitites with
72 detailed mineralogical analyses of platinum group element (PGE) alloys and base
73 metal sulfide (BMS) inclusions can provide valuable information for
74 reconstructing the ore-forming processes (Melcher 2000; Uçurum et al. 2006;
75 Rollinson 2008; Uysal et al. 2009). Chromitites commonly exhibit significantly
76 higher PGE contents compared to the peridotites hosting them, with micrometer-
77 sized PGM inclusions, such as sulfides of the laurite-erlichmanite series, alloys in
78 the Os-Ir-Ru system, and sulfarsenides of Ir, Ru, and Os, contributing to the PGE
79 budget (Tsoupas and Economou-Eliopoulos 2021).

80 Ultrahigh-pressure (UHP) mineral inclusions in mantle peridotites and
81 chromitites from several orogenic belts suggest a multistage genesis of ophiolite
82 host rocks under deep to shallow mantle conditions (Yang et al. 2014; Xiong et al.
83 2015, 2022a, b). However, the origin of podiform chromitites in subduction-
84 related environments is challenging to reconcile with the presence of UHP and
85 super-reduced (SuR) mineral phases in many chromitites (Robinson et al. 2004,
86 2015; Yang et al. 2007; Xu et al. 2009). This suggests recycling of chromitites and
87 their host rocks in upper mantle regions (Robinson et al. 2004; Yamamoto et al.
88 2009).

89 The Luobusa ophiolite in the Indus—Yarlung Zangbo suture of southern Tibet
90 was interpreted as a forearc fragment of Neo-Tethyan oceanic lithosphere (Zhou
91 et al. 1996, 2005; Bai et al. 2000; Shi et al. 2007; Yang et al., 2007). It contains the
92 largest chromite deposit in China, with reserves over several million metric tons

93 of ore, with Cr₂O₃ as high as 50 wt% and Cr₂O₃/FeO > 4 (Li et al. 1995; He et al.
94 2021). According to Zhou et al. (1996), the Luobusa ophiolite is characterized by
95 a distinctive mantle sequence comprising harzburgite and diopsidic harzburgite
96 with abundant dunite lenses and podiform chromitites. These harzburgites
97 represent the residual rocks formed after tholeiitic magma extraction and contain
98 accessory chromite grains, which exhibit variations in Cr and Al contents and low
99 Ti levels, aligning them with mid-ocean ridge basalt (MORB)-type peridotites
100 (Zhou et al. 2005). On the other hand, podiform chromitites in Luobusa likely
101 originated from the crystallization of boninitic melts during a late stage of melting
102 (Zhou et al. 1996). Similarly, several authors (e.g., Yang et al. 2007; Zhou et al. 2005;
103 Wang et al., 2010; Xu et al. 2015; Zhang et al. 2017, 2019, 2020; Xiong et al., 2022)
104 have suggested that the Luobusa ophiolite formed at a mid-ocean ridge and,
105 subsequently was partially melted to generate boninitic magmas in a SSZ setting.

106 In the Luobusa podiform chromite, researchers have discovered an array of
107 UHP minerals, including microdiamonds and coesite, as distinct inclusions (e.g.,
108 Bai et al. 2000, 2004; Yang et al. 2007; Xiong et al. 2015). This suggests that the
109 formation of chromite likely commenced at significant depths, possibly within the
110 transition zone or lower mantle (Xiong et al. 2015). The formation process of
111 Luobusa podiform chromite appears to involve both deep-seated and shallow
112 processes, potentially spanning multiple stages of evolution, including events in
113 the transition zone, mid-ocean ridges, subduction zones, and even late-stage
114 surface modifications, as discussed in Xu et al. (2015) and Xiong et al. (2015). This
115 makes the Luobusa ophiolite a case study for gaining insights into the origin and
116 evolution of significant podiform chromite deposits in forearc ophiolites.

117 In this contribution, we investigate the mineral chemistry of Luobusa
118 chromitite and its host peridotites, offering a comprehensive analysis of
119 petrographic and geochemical attributes concerning PGM and BMS inclusions. We
120 examine the complex formation process involving deep-seated and shallow
121 processes across various stages of geological evolution of significant podiform
122 chromite deposits within forearc ophiolites, positioning the Luobusa ophiolite as
123 a compelling case study in understanding the intricate dynamics shaping such
124 geological phenomena.

125 **GEOLOGICAL SETTING**

126 The Yarlung Zangbo suture zone in southern Tibet extends over 2000 km,
127 separating the Indian subcontinent from the Eurasian subcontinent. Among
128 several ophiolitic massifs, the Luobusa nappe occurs along the Yarlung Zangbo
129 suture zone and is located approximately 200 km southeast of Lhasa. It extends
130 for about 40 km along strike and is separated from Triassic flysch by a reverse
131 fault. The Luobusa ophiolite tectonically overlies the Tertiary Luobusa Formation
132 and Gangdese arc granite to the north (Fig. 1) (Yang et al. 2007). This ophiolitic
133 nappe consists of peridotite and subordinate mafic cumulates. At the base of the
134 nappe, a thin zone contains tectonically admixed volcanic rocks and cherts (Yang
135 et al. 2007). The peridotites include harzburgite, refertilized harzburgites, and
136 dunite. The mafic cumulate rocks include gabbro, wehrlite, and pyroxenite (Wang
137 et al. 1987) (Fig. 1). A dunite zone about 150 m thick underlies the ophiolitic nappe
138 and is cut by N-S normal faults.

139 In the Luobusa ophiolite nappe, chromitite ore bodies are commonly found in
140 association with harzburgite and are typically enclosed by dunitic rims, as
141 observed in previous studies (Zhou et al. 1996). These chromitite deposits occur
142 as lenticular, podiform, or irregular masses, typically measuring less than 100 m
143 in length. They are located in the upper part of the mantle section or are associated
144 with the transitional dunite (Xiong et al. 2015). Various modes of occurrence were
145 observed, including massive, nodular, and disseminated chromitite (Fig. 2). The
146 chromitite ores in Luobusa are typically 0.5 to 3 m long, although some can reach
147 up to 20 m. The ore bodies primarily consist of magnesiochromite, accounting for
148 up to 95% of the modal composition (Xiong et al. 2015). The chromitite ores are
149 surrounded by dunite, which predominantly comprises granular olivine and
150 amoeboid magnesiochromite (Fig. 2).

151 The geochronological data available for the ophiolitic rocks in the Luobusa
152 area indicate a diachronous evolutionary history. It is suggested that around 177
153 \pm 33 Ma the prevailing environment was a mid-ocean ridge setting (Zhou et al.
154 2002). A geodynamic shift occurred at \sim 126 Ma, and the ophiolites were
155 imprinted by a supra-subduction zone environment (Malpas et al. 2003). This
156 transition imitates the tectonic processes associated with the subduction of

157 oceanic crust beneath an overriding plate. During the late stages of ophiolite
158 evolution, the MORB-like mantle peridotites in Luobusa were likely fertilized by
159 melts derived from supra-subduction zone settings (e.g., Xu et al. 2011, 2023; Li et
160 al. 2012). These incompatible element-rich melts infiltrated the mantle peridotites
161 and contributed to the formation of chromitite ore bodies (Zhou et. 2014).

162

163 **SAMPLES AND METHODS**

164 *Sampling*

165 Sampling in the Luobusa region presents a unique challenge due to the
166 widespread distribution of chromite ore bodies. To date, ~ 300 chromite ore
167 bodies of varying sizes and morphologies have been discovered in this area, with
168 chromite deposits occurring across different lithological zones, as detailed in
169 Xiong et al. (2015). Our primary focus centers on specific chromitite ore bodies in
170 Luobusa, particularly the Cr-11 and Cr-31 ore bodies. These ore bodies exhibit a
171 rich variety of ore structure types, including disseminated chromitite, banded
172 chromitite, nodular, anti-nodule, and massive chromitite, among others. The
173 massive chromite displays pristine composition and textural features, which
174 qualify it to gain insights into its genesis and evolution (Xiong et al. 2015).

175

176 *Mineral chemistry*

177 Following petrographic investigation of 60 polished thin sections, the
178 mineralogical composition and textural characteristics of the studied chromitites
179 and associated peridotites were analyzed with a JEOL JXA-8100 electron
180 microprobe at the State Key Laboratory Breeding Base of Nuclear Resources and
181 Environment, East China Institute of Technology. The measuring conditions
182 included an accelerating voltage of 15 kV, beam current of 20 nA, and beam
183 diameter of 1 μm . The detection limits for elements in the chromitite grains and
184 PGM were ~0.01 wt %. Synthetic and natural metal alloys and minerals were used
185 as standards. A pure cobalt reference standard was analyzed every five analyses
186 in order to check for any drift in the analytical conditions. The BMS minerals and

187 PGM found were analyzed using the $L\alpha$ lines for Ru, Ir, Rh, Pd, Pt and As, the $M\alpha$
188 line for Os and the $K\alpha$ lines for S, Ni, Fe and Cu. A comprehensive set of standards
189 including pure metals for PGE, Ni and Cu, arsenopyrite for As, and pyrite for Fe
190 and S were used to calibrate the EPMA.

191 Because PGM typically occur as a few μm -large inclusions in chromite grains
192 in the peridotite samples (Capobianco and Drake 1990; Gonzalez-Jimenez et al.
193 20012, 2014), we used the backscattered electron images to distinguish the PGE
194 minerals, and then to determine their chemical composition (size of 10-100 μm)
195 by EMPA. Fifteen representative samples of massive chromitite were selected to
196 study the PGM inclusions. We note that several PGM grains were either too small
197 ($\leq 2 \mu\text{m}$) or inhomogeneous for quantitative determination.

198

199 *Trace element composition of pyrite inclusions*

200 The chemical compositions of pyrite inclusions were determined by the laser
201 ablation-inductively coupled plasma-mass spectrometry (LA-ICP-MS) at the
202 GEOMAR Helmholtz Centre for Ocean Research Kiel, Germany. This instrument is
203 a 193 nm Excimer laser ablation system (Coherent, GeoLasPro) that is coupled to
204 a double-focusing magnetic sector mass spectrometer (Nu Instruments, AttoM)
205 under hot plasma conditions (NAI = 24 - 35; ThO/Th = 0.016 - 0.022 %; Fietzke
206 and Frische 2016). Spot analyses were performed as 30 s ablation under Helium
207 carrier gas at a laser repetition rate of 5 Hz, a spot diameter of 44 μm , and a fluence
208 of 2 and 5 J cm^{-2} for sulfides and silicate glasses, respectively. The USGS glass
209 standard BHVO-2G (Wolf and Wilson 2007), the USGS sulfide standard MASS-1
210 (Wilson et al. 2002), and the synthetic sulfide standard PGE-Ni7b (Wohlgemuth-
211 Ueberwasser et al. 2007) were used as reference materials. The NISTSRM610
212 glass (Wise and Watters 2012) was used for the sake of mass calibration, but due
213 to the lack of suitable reference values for S, Ru, Os, Ir and Hg, the MASS-1 was
214 used to calibrate S, Ir and Hg and PGE_Ni7b to calibrate Ru and Os. 60 - 80 s of gas
215 background data were collected prior to each ablation. The data evaluation was
216 performed by applying the linear regression slope method proposed by Fietzke et
217 al. (2008). Data are corrected for the following interferences: $^{65}\text{CuH}^+$ on $^{66}\text{Zn}^+$;
218 $^{63}\text{Cu}^{40}\text{Ar}^+$ on $^{103}\text{Rh}^+$; $^{65}\text{Cu}^{40}\text{Ar}^+$ on $^{105}\text{Pd}^+$ and $^{115}\text{Sn}^+$ on $^{115}\text{In}^+$. The exact argide

219 and hydride formation rates were determined by ablating elemental Cu (line-scan,
220 60 - 120 s, 32 μm spot size, 5 J cm^{-2}). Fe contents in pyrite grains as determined by
221 the EPMA were used for internal standardization of the LA-ICP-MS data.

222

223

224 *Bulk-rock PGE geochemistry*

225 The PGE concentrations in the peridotite and chromitite samples were
226 determined at the National Research Center of Geoanalysis, Chinese Academy of
227 Sciences (CAS) using the NiS fusion pre-concentration technique followed by ICP-
228 MS measurement. The CAS uses a modified NiS-fire assay method (Sun and Sun
229 2005; Zhou et al. 2005) in which the samples are mixed with sodium carbonate,
230 sodium borate, borax, glass powder, nickel powder, iron powder, and sulfur. The
231 mixtures are transferred into fire-clay crucibles, with an appropriate amount of
232 ^{190}Os spike solution and covered with a thin layer of $\text{Na}_2\text{B}_4\text{O}_7$. After fusing at
233 1150°C for ~ 1 h and drying under an infrared lamp, the crucibles are cooled and
234 the Ni-Fe buttons are removed. The buttons are then placed in a glass beaker
235 containing 60 mL H_2O for a minimum of 10 h. To better dissolve the button, about
236 30 mL HCl is added and the beaker is heated at $\sim 110^\circ\text{C}$ for ~ 30 min, and left to
237 cool 10 h until the solution becomes clear and the residue is seen. The solution is
238 then filtered using a millipore filter membrane (diameter 25 mm, 0.45 μm), and
239 then the precipitate is collected and washed five times with ~ 15 mL water. The
240 residue, together with the membrane, is transferred to a 7 mL Teflon beaker,
241 sealed together with 1 mL HCl + 1 mL H_2O_2 , and heated at $\sim 110^\circ\text{C}$ for 1.5 h. Upon
242 cooling to room temperature, the beaker was opened and the solution was
243 transferred and diluted with H_2O to a total volume of 10 mL in preparation for ICP-
244 MS analysis (Sun et al. 1998a, b; Sun and Sun 2005). The detection limit was 0.2
245 ng/g for Pt and Pd, 0.001 ng/g for Ir, Rh, and Os, and 0.1 ng/g for Ru. The precision
246 of the analyses was estimated to be better than 5% for Rh, Pd, and Ir, and 10% for
247 the other elements.

248

249 **RESULTS**

250 *Mineralogical characteristics of PGM and BMS inclusions*

251 Numerous BMS sulfide inclusions were observed by backscattered electron
252 images in the examined samples of the Luobusa massive chromitites. Abundant
253 pyrite, arsenopyrite, sphalerite, galena, tennantite-(Zn), pentlandite, tetrahedrite-
254 (Zn), heazlewoodite, antimonite, spionkopite, millerite, and chalcocite inclusions
255 were observed in the Luobusa chromitites (Fig. 3; Figs. S1-S5). Most pyrite
256 inclusions (Fig. 3) have stoichiometric compositions and Fe/S ratios between 0.52
257 and 0.54 (Table S1). Minor amounts of other elements such as Cd, Cu, Pb were
258 above the detection limits in some inclusions. Arsenopyrite (Table S1) shows
259 variations in the atomic (Fe+Mo)/(S+As) ratios from 0.52 to 0.56 and
260 stoichiometric composition. Some analyses also contain minor amounts of Bi and
261 Ag. Sphalerite shows an atomic (Zn+Fe)/S variation of 0.97 to 1.09 with a
262 stoichiometric composition of $Zn_{0.9}S$. Cadmium, Cu, and Ge are present in trace
263 quantities. Galena, tennantite-(Zn), and tetrahedrite-(Zn) occur as inclusions in
264 the pyrite grains. Galena has an atomic (Pb+Fe)/S ratio of 1.07 to 1.11 with a
265 composition of $Pb_{1.09}S$. Tennantite-(Zn) shows variations in the atomic
266 (Fe+Ni+Zn)/S ratios from 0.71 to 1.19 and a composition formulated as
267 $Cu_{10.6}Zn_{1.8}Fe_{0.6}As_{3.4}S_{13}$. Tetrahedrite-(Zn) shows an atomic (Fe+Ni+Zn)/S variation
268 of 1.13 to 1.24 and a composition of $Cu_{10}Zn_{1.9}Fe_{0.5}Sb_3S_{13}$. Heazlewoodite inclusions
269 ($Ni_{1.4}Fe_{1.2}S_2$) show an atomic (Fe+Ni+Zn)/S of 1.32 (Table S1). Antimonite shows
270 an atomic (Sb+Cu)/S variation of 0.66 to 0.67 and has a stoichiometric
271 composition of $Sb_2Cu_{0.1}S_3$. Millerite shows an atomic (Ni+Fe)/S variation between
272 1.09 and 1.12. In addition, micron-sized augite, microcline and phlogopite were
273 observed in the large pyrite inclusions (Fig. 4; Table S2).

274 Abundant particles of PGM and alloys were observed in the examined thin
275 sections. PGM inclusions in the Luobusa chromitites include RuS_2 (laurite), (Ru, Os,
276 Ir) S_2 , cuproiridsite, and ruthenarsenite (Ru, Os, Ir) S_2 . These inclusions are

277 commonly < 100 μm in size and locally intergrown with amphibole and phlogopite.
278 Most of the PGM inclusions (< 10 μm -across) are euhedral crystals, while the BMS
279 inclusions are subhedral to anhedral grains. Some of monomineralic and
280 composite grains are PGM and are associated with silicate minerals (Fig. S1, Table
281 S3). The (Ru, Os, Ir) S_2 series minerals exhibit a wide range of these three elements
282 (Table S3, Fig. 5), for example 5.97 to 41.10 wt% Ru, 5.44 to 63.49 wt% Os, and up
283 to 23.36 wt% Ir. RuS_2 was also observed as euhedral inclusions ($\text{Ru}_{0.27}\text{S}_2$ to $\text{Ru}_{0.96}\text{S}_2$)
284 in Luobusa chromitite (Fig. 5, Table S3). The associated Ru-Os-Ir phases may
285 indicate that some RuS_2 inclusions (5-80 μm) are of late metasomatic origin. The
286 RuS_2 inclusions have variable S contents ranging from 37.5 to 42.6 wt% and Ru
287 contents ranging from 29.9 to 60.39 wt%, as well as a small amount of Ir and As.
288 In addition to the PGE alloys, a large number of PGM were observed in the Luobusa
289 chromitites, including Pt-Fe-Ir, Pt-Fe-Rh, Pt-Pd-Fe, Os-Ru-Ir, Pt-Pd-Fe-Ir, Pt-Pd-Fe-
290 Cu, and Os-Ir (Figs. 5, 6, Figs. S1, S5; Table S4). The Os-Ir alloy occurs commonly as
291 small particles (1-3 μm) and is considered the most abundant alloy in the studied
292 samples. Other inclusions with Ir- and Cu-sulfide compositions exhibit
293 idiomorphic habits (Fig. 5, Figs. S6, S7).

294 The EPMA data indicate that the compositions of Os-Ir-Ru alloys vary widely,
295 with or without traces of Fe and Ni. The Os content ranges from 14.68 to 48.46
296 wt%, Ir from 20.94 to 76.11 wt%, and Ru from 1.02 to 56.72 wt%, indicating an
297 osmium-rich iridium sulfide. In contrast, Fe-Ni alloys most commonly occur in
298 fractures or as interstitial fillings (Fig. 5) between chromite grains. Their
299 compositions are uniform (Table S5) and are formulated as $\text{Ni}_{2.4}\text{Fe}_{0.8}$, typical of
300 awaruite (ideally Ni_3Fe).

301

302 *Trace element abundances in pyrite inclusions*

303 LA-ICP-MS analysis of pyrite inclusions shows a proportional covariance between
304 Co-Ni, Cu-Zn, and Cu-Pb. Ag contents are also positively correlated with Au, Te, Sb,

305 and Cu contents. The Cu and As contents in the analyzed pyrite range from < 1 to
306 6038 ppm and from 1 to 16964 ppm, respectively. The average values are 258 ppm
307 (Cu) and 3113 ppm (As). The Pb content in the pyrite ranges from 0.1 to 11846
308 ppm, with an average value of 236 ppm. Gold values in the analyzed pyrite
309 inclusions are remarkably high, ranging from 13.4 to 150 ppm, with an average
310 value of 119 ppm. In general, the Pb and Zn contents in the pyrite were positively
311 correlated, as are Au and Ag (Fig. 7). The As content ranges from 0 to 13644 ppm
312 (Table S6).

313

314 *Bulk rock PGE concentrations*

315 Whole-rock PGE concentrations in 50 samples of Luobusa podiform chromitites
316 and peridotites show significantly high total PGE contents in chromitites (40.2-
317 333.6 ppb), with an average value of 146.3 ppb (Table S7). Total PGE contents in
318 peridotites range from 0.3 to 63.4 ppb, with an average value of 33.7 ppb (Table
319 S7). The studied chromitites feature high (Ru/Pt)_N ratios (8.1 to 90.1). The
320 chromitites have extremely low (Pd/Ir)_N values (0.01-0.30) compared to the
321 chondrite value of 1.01 (McDonough and Sun 1995; Fig. 9).

322

323

324 **DISCUSSION**

325 *Sulfide inclusions*

326 The presence of unusual mineral phases (e.g., arsenotučekite (Ni₁₈Sb₃AsS₁₆),
327 eliopoulosite (V₇S₈), tsikourasite (Mo₃Ni₂P_{1+x}) and grammatikopoulosite (NiVP))
328 in podiform chromitites may reflect their formation under specific conditions
329 related to variations in oxygen fugacity (fO_2) and sulfur fugacity (fS_2) (e.g., Bindi et
330 al. 2020a, b). In the Luobusa peridotites and chromitites, intergrowths of sulfide
331 and platinum group mineral phases may also be related to variations in fO_2 and fS_2

332 (e.g., Klein and Bach 2009; Zhu and Zhu 2019).

333 The trace element geochemistry of pyrite in Luobusa chromitite highlights a
334 possible contrast between crustal contamination and mantle source influences.
335 While some areas of individual pyrite inclusions exhibit enrichments in Ni, Co, Ag
336 and Au, other portions reveal elevated levels of As, Cu, Zn, Pb, Cd, Sn, and W,
337 suggesting contamination from crustal materials. The presence of silicate
338 inclusions, such as pyroxene, and potentially other sulfide phases within the pyrite
339 inclusions, likely contributed to the observed heterogeneity in their trace element
340 composition. Figure 7 shows a notably positive correlation between Pb and Zn, as
341 well as Au and Ag, suggesting hydrothermal or metasomatic process may have
342 been active during pyrite formation (Zhu and Zhu 2019).

343

344 *PGM inclusions*

345 The mineralogy and textures of PGM are commonly utilized to understand the
346 origin and evolution of chromitites, as well as to determine parameters such as
347 temperature, oxygen fugacity (fO_2), and sulfur fugacity (fS_2) of the parent melt
348 (Garuti et al. 1999; González-Jiménez et al. 2012, 2014; Xiong et al. 2021). In the
349 Luobusa chromitite, PGM inclusions intergrown with amphibole and phlogopite
350 likely represent primary composite inclusions derived from a hydrous melt (see
351 Fig. 3 and Fig. S1). The observed chemical variations, irregular morphologies, and
352 alteration rims may be attributed to post-crystallization alteration or
353 metamorphism processes (Stockman and Hlava 1984; Proenza et al. 2008).

354 Within the Luobusa chromitites, the PGM are disseminated and occur as
355 single-phase (Fig. 5a-c), two-phase, or polyphase hypidiomorphic or xenomorphic
356 inclusions (Fig. 5d-i). In some examples, symplectite textures with microscopic
357 multiphase (Fe-Ni, Ir-Fe) pseudo-structures in Os-Ir, Os-Ir-As, Lrt, Os-Al, and Ir-Al
358 matrices (Fig. 5d, e, f) may suggest decompression under high-pressure/high-
359 temperature conditions during the evolution of the Luobusa chromitites through
360 recycling in deeper mantle levels (e.g., White and Powell 2011; Groppo et al. 2015).

361 The identified PGM exhibit compositions rich in Ir-Os-Ru or Pt-Rh-Os (Fig. 6a,
362 b), with their diversity in PGE mineralogy closely aligning with the immiscibility
363 gap, which is believed to narrow at elevated temperatures. This diversity in PGE
364 mineralogy, coupled with the chemical composition variations observed in
365 chromite grains within the Luobusa chromitites, indicates potential differences in
366 the parent magma(s). Such distinctions may arise from varying degrees of partial
367 melting and melt-rock interactions (e.g., Economou-Eliopoulos et al., 2017).
368 Consequently, these features likely reflect fluctuations in temperature, oxidation
369 state, and/or sulfur fugacity (fS_2) (e.g., Garuti et al., 1999; Ahmed and Arai, 2002).

370 The formation and stability of platinum group minerals in chromitites are
371 predominantly controlled by the sulfur fugacity and temperature of the melt (Augé
372 1988). Luguét and Reisberg (2016) proposed that Ir-Pt-(Os) alloys in mantle
373 peridotite associated with BMS likely originated from PGE-bearing monosulfide
374 solid solution (MSS) that underwent desulfurization during high-temperature
375 partial melting. Ir-Pt-(Os) release from BMS could also result from mantle redox
376 changes or interactions with S-undersaturated melt/fluids. On the other hand,
377 experiments and observations in the Fe-Cu-S-(Pt+As) system and in PGE ores in
378 the Bushveld Complex suggest that Pt-rich nanoparticles may form before MSS
379 crystallization (Helmy et al. 2013; Wirth et al. 2013; Junge et al. 2015). Finnigan et
380 al. (2008) provided evidence for the direct crystallization of Ir-Pt nanocrystals,
381 approximately 700 nm in diameter, from basaltic melt. The experimental work was
382 conducted under the relevant conditions for chromite deposit formation in the
383 upper mantle, specifically at approximately 0.5 GPa, temperatures of around
384 1300–1400°C, and with fO_2 at fayalite-magnetite-quartz (FMQ) buffer (Stockman
385 and Hlava 1984; Johnson et al. 1992; Zhu and Zhu 2019).

386 Some PGM can be incorporated into chromitites through reactions between
387 the melt and peridotite. Multiple episodes of melt extraction can lead to a gradual
388 decrease in melt fS_2 , resulting in the decomposition of PGE sulfides and the
389 formation of Ru-osmite and Os-Ir alloys while chromite crystallizes. This
390 mechanism can account for the variable mineralogical characteristics of PGM and
391 the wide range of Re-depletion model ages (TRD) (up to ~ 234 Ma) and magmatic
392 events observed in chromitites, which are distinct from the age of the Luobusa
393 ophiolite (177 ± 33 Ma; Zhou et al. 2002; Shi et al. 2007; McGowan et al. 2015).

394 The Os-Ir alloys tend to form at earlier paragenetic stages and under higher
395 temperature and pressures compared to sulfides and sulfarsenides (e.g., laurite-
396 erlichmanite series) (Augé 1988; Andrews and Brenan 2002a,b; Gonzalez-Jimenez
397 et al., 2012, 2014; Uysal et al. 2015). This implies that the fS_2 was initially low and
398 increased significantly at lower temperatures, allowing the crystallization of
399 laurite and erlichmanite. Experimental research has demonstrated that
400 erlichmanite can coexist in equilibrium with Os-Ir alloys at fS_2 values ranging from
401 -1 to +2 (Barnes et al. 2001). Based on the PGE mineralogy group include laurite,
402 Os-Ir-Ru alloys, erlichmanite, and PGE-BM sulfides and theoretical meta-sulfide
403 equilibrium curves for Ru, Ir, Os, and Ni as a function of fS_2 and temperature (see
404 Fig. S8), it is suggested that the Luobusa chromitites and their associated PGM
405 formed under low fS_2 conditions, within a temperature range of 1300°C to 1050°C,
406 indicating upper mantle origins (Zhu and Zhu 2019 and references therein).

407

408 *PGE geochemistry*

409 The geochemical characteristics of PGE are frequently employed to elucidate
410 various petrological processes involved in the formation of podiform chromitite
411 (Barnes et al. 1985). The behavior of PGE during the crystallization of host
412 chromitite is significantly influenced by two key mechanisms: the degree of mantle
413 partial melting to form the source magma and the extent of crystal fractionation
414 during the magma evolution (e.g., Stockman and Hlava 1984; Legendre and Augé
415 1986). These mechanisms are central to understanding the distribution and
416 behavior of PGE within the chromitite. The chondrite-normalized PGE patterns of
417 mantle peridotite xenoliths and Alpine peridotites typically exhibit flat profiles (Xu
418 and Liu 2019; Xu et al. 2020; Liu et al. 2020). The Pd/Ir ratio, a measure of
419 PPGE/IPGE fractionation, can be used as an indicator of melt depletion and
420 metasomatism (e.g., Liu et al. 2010; Pearson et al. 2004). The continental and
421 oceanic basalts exhibit steeply sloping positive patterns with Pd/Ir ratios ≤ 100 ,
422 reflecting more pronounced PGE differentiation in the parental magmas (Xu and
423 Liu 2019; Xu et al. 2020; Liu et al. 2020).

424 Leblanc (1991) suggested that the PGE concentrations in ophiolite-associated
425 podiform chromitites increase as Pd/Ir ratios decrease. Chondrite-normalized

426 PGE patterns of ophiolites typically display a positive slope and variable Pd/Ir
427 ratios, whereas associated chromitites exhibit a negative slope and Pd/Ir ratios
428 typically around 0.1 (Zhou and Robinson 1994). The total PGE (Σ PGE)
429 concentrations in both the Luobusa high-Cr and high-Al podiform chromitites
430 range from tens to thousands of ppb (Fig. 8). In the chondrite-normalized PGE
431 patterns, the high-Cr chromitites from Luobusa consistently exhibit significant
432 depletion of PPGE relative to the IPGE (Fig. 8). The geochemical characteristics of
433 Luobusa dunite are similar to those of the high-Al chromitite (Fig. 8b), showing
434 diverse behavior with varying degrees of incompatibility or preferential varying
435 removal, typically in the order of rhenium (Re) > Pd > Pt > Ir > Ru > Os (Pearson et
436 al. 2004).

437 The absolute abundances of the PGE and their normalized patterns, as well
438 as the chemical composition of Cr spinel in podiform chromitites, are sensitive
439 indicators of mantle partial melting, primary melt composition, and melt
440 saturation with volatile components (Zaccarini et al. 2005). The Luobusa
441 chromitites commonly described as high-Cr chromitite (Xiong et al. 2015), which
442 are enriched in the Ir subgroup (IPGE = Os, Ir, Ru) relative to the Pd subgroup
443 (PPGE = Rh, Pt, Pd) and display negatively-leaning chondrite-normalized PGE
444 patterns typical of ophiolitic high-Cr chromitites elsewhere (Melcher and Meisel
445 2004; Fig. 8). Dunite and harzburgite of Luobusa ophiolite have variable (Ru/Pt)_N
446 ratios ranging from 0.25 to 8.37, 0.12 to 6.55, respectively. These variations
447 indicate the percolation of sulfide-rich melts enriched in PGE (Figs. 3 and 4).
448 Similar to most high-Cr chromitites, the Luobusa chromitite samples show a
449 consistent relationship between (Pt/Ir)_N and (Pd/Ir)_N ratios. The majority of data
450 points align along a common fractional melting curve in the (Pt/Ir)_N versus
451 (Pd/Ir)_N space (Fig. 9a). In contrast to abyssal peridotites, forearc peridotites
452 exhibit depletion of osmium (Os) and low Os/Ir ratios. The higher Os/Ir ratio (e.g.,
453 5.9 in the chromitite sample 11Y910-4) can indicate processes like partial melting
454 or fractional crystallization of peridotites (Table S7). In contrast, the lower Os/Ir
455 ratio (e.g., 1.108 in the dunite sample 11Y-1107) suggests a different geological
456 history, possibly influenced by sulfide segregation or other processes (Fig. 9c). The
457 studied chromitites have undergone a significant loss of Os during sulfide
458 dissolution (e.g., Liu et al. 2010).

459 The Luobusa chromitites have Cr#s = 76-83 (Xiong et al. 2015). Compared to
460 other high-Cr and high-Al chromitites, the Luobusa chromitites display contrasting
461 fractionation trends (Fig. 9b), while dunite samples show a similar trend to abyssal
462 peridotites. Os, present in highly siderophile element (HSE) mineral phases in the
463 mantle wedge, can be mobilized by sulfide-undersaturated melt or fluid
464 components, such as those with high oxygen fugacity (fO_2) and chloride-rich
465 compositions derived from subducted slabs (Liu et al. 2010; Foustoukos 2019; Xu
466 et al. 2020). This mobilization of Os relative to Ir, Ru, and Pt leads to significant
467 fractionation, resulting in low Os/Ir ratios and overall abundances of total PGE in
468 peridotites (Liu et al. 2010) (Figs. 5, 6; Fig S1) as observed in the Luobusa ophiolite.
469 In contrast, the chromitites have Os/Ir ratios higher than the peridotites (Fig. 9c).
470

471 *Genesis of the PGM and BMS inclusions*

472 The formation of Luobusa podiform chromitites is believed to result from multiple
473 stages of partial melting and mantle metasomatism, include the MOR and SSZ
474 processes (Bai et al. 2000; Robinson et al. 2004; Xiong et al. 2015, 2022a, b). The
475 heterogeneity of PGE composition and Os isotopes reflects the mixing of melts
476 derived from different mantle source regions during multiphase metamorphism
477 or migration of chromitite to different mantle levels. According to Zhou et al.
478 (1996), the multi-stage crystallization and re-equilibrium of chromite may have
479 led to PGM dissolution and reprecipitation, suggesting that some PGM inclusions
480 are secondary. Nonetheless, euhedral PGM inclusions and silicate exsolutions in
481 chromite may reflect deeper mantle depths (e.g., Yang et al. 2007).

482 The PGE-bearing sulfides and sulfarsenides occur as euhedral inclusions,
483 while BMS typically form anhedral or amoeboid particles interstitially between
484 chromitite grains. In some cases, micro-diamond inclusions in Os-Ir alloys were
485 reported in the Luobusa chromitite (Yang et al. 2007). Laurite and Os-Ir-Ru alloys
486 commonly form during the early stages of magma crystallization at high
487 temperatures ($\sim 1300^\circ\text{C}$) and low sulfur fugacity (fS_2) (e.g., Zaccarini et al. 2005;
488 Fig. S8). IPGE partition favorably into BMS when they crystallize from S-rich melts,
489 which tend to retain Ag, and possibly Au and semi-metals (As, Sb, Pb, Bi)
490 fractionate into the co-existing sulfur-rich melt.

491 During mantle upwelling, the BMS and laurite-erlichmanite solid-solution
492 crystallize at lower temperatures and higher levels of fS_2 (Fig. 10) (Klein and Bach
493 2009). The abundant BMS inclusions, including millerite and heazlewoodite, in
494 Luobusa chromite may indicate high fS_2 conditions (\sim -11). Also, the coexistence
495 of pentlandite and heazlewoodite has been explained by the establishment of
496 highly reducing conditions under low temperatures (Klein and Bach 2009).
497 Millerite inclusions in chromite may imply that crystallization occurred below the
498 heazlewoodite-millerite buffer and continued to low temperatures ($< 1000^\circ\text{C}$) and
499 high fS_2 conditions (Fig. 10). Sulfides with low PGE contents can be explained by
500 the late paragenesis of some of these sulfides. This is similar to the Bacuri complex
501 in Amapa of northeastern Brazil (Prichard et al. 2001; Zhu and Zhu 2019), in which
502 the PGE were concentrated in chromitite and sulfide-bearing serpentinite, where
503 pentlandite is partially altered to millerite, maucherite, and gersdorffite. The
504 irarsite formed at the final stage of hydrothermal processes with the introduction
505 of As, Ir, and Os, which are associated with serpentine, chlorite, and base metal
506 minerals (Fig. 11).

507 The genesis of the Luobusa chromitite unveiled a complex interplay of
508 geological processes (Fig. 11). Euhedral PGE-bearing sulfides and sulfarsenides
509 contrasted with anhedral or amoeboid BMS particles, indicating distinct
510 crystallization environments. Early magma crystallization at high temperatures
511 gave rise to laurite and Os-Ir-Ru alloys, with subsequent BMS crystallization
512 occurring under lower temperatures and higher sulfur fugacity. The presence of
513 millerite and heazlewoodite suggested highly reducing conditions, while the late-
514 stage introduction of As, Ir, and Os was indicative of hydrothermal processes. This
515 dynamic evolution, marked by interactions between mantle upwelling,
516 suprasubduction processes, and fluid intrusion, resulted in the formation of
517 chromian spinels, PGE-bearing sulfides, and PGM at high temperatures. The
518 integration of geochemical data and isotopic characteristics further supported a
519 multifaceted genesis involving mantle partial melting, melt-peridotite interaction,
520 and slow spreading ridge dynamics, ultimately shaping the unique composition
521 and structure of the Luobusa chromitite.

522

523 **IMPLICATIONS**

524 The mineralogical and geochemical characteristics of the Luobusa chromitite and
525 ophiolite suggest an intricate geological history shaped by a dynamic interplay of
526 factors. Abundant occurrences of PGM and BMS inclusions underscore a multi-
527 stage genesis involving processes like partial mantle melting, melt-rock
528 interactions, and fluctuations in oxygen and sulfur fugacity. The geochemical
529 fingerprints, encompassing the patterns of PGE, provide substantial evidence for
530 the transformation of the Luobusa ophiolite from a sub-ridge environment to a
531 supra-subduction zone setting.

532 The bulk-rock geochemical attributes of the Luobusa chromitite align closely
533 with those of forearc supra-subduction zone (SSZ) settings, implying a
534 compositional influence from both mantle and crustal melts. Additionally, the
535 trace element characteristics of pyrite inclusions bear striking resemblances to
536 sulfides found in MORB and OIB rocks, accentuating the complex intermingling of
537 various magmatic sources.

538 The observed diversity in PGM and BMS inclusions, coupled with the
539 geochemical features of the chromitite, advocate for an intricate genesis
540 characterized by mantle partial melting, assimilation of crustal components, and
541 extensive melt fractionation. The coexistence of well-formed Os-Ir alloys alongside
542 interstitial BMS implies conditions of elevated temperatures and low fS_2 during
543 earlier stages. The presence of sulfarsenides as small inclusions in pyrite point
544 towards lower temperatures and higher fS_2 values during later paragenetic phases.
545 This multi-faceted geological history exemplifies the intricate nature of chromitite
546 formation in the Luobusa ophiolite.

547

548 **Acknowledgments**

549 This work was co-supported by the National Key Research and Development
550 Project of China (No. 2023YFF0804401), the National Natural Science Foundation
551 of China (NNSFC; Project No. U2344202, 42172069, 92062215), the Second
552 Tibetan Plateau Scientific Expedition and Research Program (No. 2019QZKK0801),
553 and the China Geological Survey (CGS; Project No. DD20230340, DD20221630).

554 Basem Zoheir acknowledges the DFG (Deutsche Forschungsgemeinschaft, German
555 Research Foundation) for enabling this research (Project No. 457324982). Paul
556 Tomascak (AM Associate Editor), Lisa Ziemann, and an anonymous reviewer are
557 thanked for their thorough reviews and insightful comments that improved the
558 clarity of this contribution.

559

560 **Appendix A. Supplementary Material**

561

562 This section provides a brief overview of the supplementary files associated with
563 this paper, offering readers additional information to complement the main text.
564 In Fig. S1, backscattered electron (BSE) images offer insights into the morphology,
565 texture, and mineral assemblage of the discovered PGM, BMS, and silicates within
566 the Luobusa chromitite in Tibet. Fig. S2 to Fig. S6 feature detailed mapping of
567 various mineral intergrowths and inclusions, shedding light on their spatial
568 distribution within the chromitite. Additionally, Fig. S7 showcases the different
569 PGE-bearing alloy inclusions in the chromitite. Finally, Fig. S8 places the
570 crystallization conditions for melt-sulfide into a thermodynamic context, as
571 referenced from Uysal et al. 2015.

572 Furthermore, this appendix contains essential supplementary tables,
573 including Table S1 to Table S7, which present representative compositions of
574 various minerals, inclusions, and alloy phases within the Luobusa chromitite,
575 along with trace element data. This supplementary material is indispensable for a
576 comprehensive understanding of the research presented in this paper.

577

578

579 **References**

- 580 Ahmed, A.H. and Arai, S. (2002) Unexpected high-PGE chromitite from the deeper
581 mantle section of the northern Oman ophiolite and its tectonic implications.
582 *Contributions to Mineralogy and Petrology*, 143, 263-278
- 583 Andrews, D.R. and Brenan, J.M. (2002b) Phase-equilibrium constraints on the
584 magmatic origin of Laurite+ Ru–Os–Ir alloy. *The Canadian Mineralogist*, 40(6),
585 1705–1716.

- 586 Andrews, D.R.A. and Brenan, J.M. (2002a) The solubility of ruthenium in sulfide
587 liquid: Implications for platinum group mineral stability and sulfide melt-
588 silicate melt partitioning. *Chemical Geology*, 192(3-4), 163–181.
- 589 Arai, S. and Miura, M. (2016) Formation and modification of chromitites in the
590 mantle. *Lithos*, 264, 277–295.
- 591 Arai, S. (1997) Origin of podiform chromitites. *J. Asian Earth Sci.* 15, 303–310.
- 592 Augé, T. (1988) PGM in the Tiebaghi and Vourinos ophiolitic complexes: genetic
593 implications. *Canadian Mineralogist*, 26, 177–192.
- 594 Bai, W.J., Zhou, M.F., Robinson, P.T., et al. (2000) Origin of podiform chromitites,
595 diamond and associated mineral assemblage in the Luobusa ophiolite, Tibet.
596 Beijing: Seismological Press, 1-98 (in Chinese with English abstract).
- 597 Bai, W.J., Yang, J.S., Shi, N.C., Fang, Q.S., Dai, M.Q., Xiong, M. and Yan, B.G. (2004).
598 A discovery of ultrahigh pressure minerals: wustite and native iron from the
599 mantle ophiolite, at Luobusa, Xizang. *Geological Review*, 50(2) : 184 –
600 188 (in Chinese with English abstract)
- 601 Barnes, S.J. and Roeder, P.L. (2001) The range of spinel compositions in terrestrial
602 mafic and ultramafic rocks. *Journal of Petrology*, 42, 2279–2302.
- 603 Barnes, S.J., Naldrett, A.J. and Gorton, M.P. (1985) The origin of the fractionation of
604 platinum-group elements in terrestrial magmas. *Chemical Geology*, 53, 303–
605 323.
- 606 Becker H., Horan M. F., Walker R. J., Gao S., Lorand J. P. and Rudnick R. L. (2006)
607 Highly siderophile element composition of the Earth's primitive upper mantle:
608 constraints from new data on peridotite massifs and xenoliths. *Geochimica et*
609 *Cosmochimica Acta*, 70, 4528–4550
- 610 Bindi, L., Zaccarini, F., Bonazzi, P., Grammatikopoulos, T. and Garuti, G. (2020a)
611 Eliopoulosite, V_7S_8 , a new sulfide from the podiform chromitite of the Othrys
612 ophiolite, Greece. *Minerals*, 10(3), 245.
- 613 Bindi, L., Zaccarini, F., Ifandi, E., Tsikouras, B. and Mauro, D. (2020b)
614 Grammatikopouosite, NiVP, a new phosphide from the chromitite of the

- 615 Othrys ophiolite, Greece. Minerals, (10),131.
- 616 Cabri, L.J. (2002) The platinum-group minerals. In: Cabri, L.J. (Ed.), The Geology,
617 Geochemistry, Mineralogy and Mineral Beneficiation of Platinum-Group
618 Elements, Canadian Institute of Mining Metallogeny and Petroleum, Special,
619 54,
- 620 Capobianco, C.J. and Drake, M.J. (1990) Partitioning of ruthenium, rhodium, and
621 palladium between spinel and silicate melt and implications for platinum
622 group element fractionation trends. *Geochimica et Cosmochimica Acta*, 54,
623 869–874.
- 624 Day, J. M. D., Walker, R. J. and Warren, J.M. (2017) ^{186}Os - ^{187}Os and highly siderophile
625 element abundance systematics of the mantle revealed by abyssal peridotites
626 and Os-rich alloys. *Geochimica et Cosmochimica Acta*, 200, 232–254.
- 627 Dickey, J.S. (1975) A hypothesis of origin for podiform chromite deposits.
628 *Geochimica et Cosmochimica Acta*, 39(6), 1061–1074.
- 629 Economou-Eliopoulos, M., Eliopoulos, D.G. and Tsoupas, G. (2017) On the diversity
630 of the PGE content in chromitites hosted in ophiolites and in porphyry-Cu
631 systems: Controlling factors. *Ore Geology Reviews*, 88, 156-173.
- 632 Fietzke J., Liebetrau, V., Günther, D., Gürs, K., Hametner, K., Zumholz, K., Hansteen,
633 T.H. and Eisenhauer, A. (2008) An alternative data acquisition and evaluation
634 strategy for improved isotope ratio precision using LA-MC-ICP-MS applied to
635 stable and radiogenic strontium isotopes in carbonates. *Journal of Analytical*
636 *Atomic Spectrometry*. 23(7), 955–961.
- 637 Fietzke, J. and Frischee, M. (2016) Experimental evaluation of elemental behavior
638 during LA-ICP-MS: influences of plasma conditions and limits of plasma
639 robustness. *Journal of Analytical Atomic Spectrometry*. 31(1), 234–244.
- 640 Finnigan, C.S., Brenan, J.M., Mungall, J.E. and McDonough, W.F. (2008). Experiments
641 and models bearing on the role of chromite as a collector of platinum group
642 minerals by local reduction. *Journal of Petrology*, 49, 1647–1665.
- 643 Fischer-Gödde, M., Becker, H. and Wombacher, F. (2011). Rhodium, gold and other

- 644 highly siderophile elements in orogenic peridotites and peridotite xenoliths.
645 *Chemical Geology*, 280(3–4), 365–383
- 646 Foustoukos, D.I. (2019) Hydrothermal Oxidation of Os. *Geochimica et*
647 *Cosmochimica Acta*, 255, 237-246.
- 648 Garuti, G., Zaccarini, F., Moloshag, V. and Alimov, V. (1999) Platinum-group
649 minerals as indicators of sulfur fugacity in ophiolitic upper mantle: An
650 example from chromitites of the Ray-Iz ultramafic complex (Polar Urals,
651 Russia). *Canadian Mineralogist*, 37, 1099–1116.
- 652 Garuti, G., Naldrett, A.J. and Ferrario, A. (1990) Platinum-group elements in
653 magmatic sulfides from the Ivrea Zone: Their control by sulfide assimilation
654 and silicate fractionation. *Economic Geology*, 85, 328-336.
- 655 González-Jiménez, J.M., Griffin, W.L., Gervilla, F., Kerestedjian, T.N., O'Reilly, S.Y.,
656 Proenza, J.A., Pearson, N.J. and Sergeeva, I. (2012) Metamorphism disturbs the
657 Re-Os signatures of platinum-group minerals in ophiolite chromitites.
658 *Geology*, 40, 659–662.
- 659 González-Jiménez, J.M., Griffin, W.L., Gervilla, F., Proenza, J.A., O'Reilly, S.Y. and
660 Pearson, N.J. (2014) Chromitites in ophiolites: how, where, when, why?, Part
661 1. A review and new ideas on the origin and significance of platinum-group
662 minerals. *Lithos*, 189, 127–139.
- 663 Groppo, C., Rolfo, F., Liu, Y. C., Deng, L. P., and Wang, A. D. (2015) P-T evolution of
664 elusive UHP eclogites from the Luotian dome (North Dabie Zone, China): How
665 far can the thermodynamic modeling lead us?. *Lithos*, 226, 183–200
- 666 Haller, M. B., O'Driscoll, B., Day, J. M. D., Daly, J. S., Piccoli, P. M., and Walker, R. J.
667 (2021). Meter-scale chemical and isotopic heterogeneities in the oceanic
668 mantle, Leka ophiolite complex, Norway. *Journal of Petrology*.
669 <https://doi.org/10.1093/petrology/egab061>
- 670 He, Y., Zhu, X.K., She, Y.W., Ma, J.X., Sun, J., Gao, Z.F., Wan, H.Q. and Chen, Y.L. (2021)
671 Mechanism of formation of podiform chromitite: Insights from the oxidation
672 states of podiform chromitites and host peridotites from the Luobusa

- 673 ophiolite, southern Tibet. *Ore Geology Reviews* 139, 104483.
- 674 Helmy, H. M., Ballhaus, C., Fonseca, R. O. C. and Nagel, T. J. (2013) Fractionation of
675 platinum, palladium, nickel, and copper in sulfide–arsenide systems at
676 magmatic temperature. *Contributions to Mineralogy and Petrology*, 166,
677 1725-1737.
- 678 Junge, M., Wirth, R., Oberthür, R., Melcher, F. and Schreiber, A. (2015) Mineralogical
679 siting of platinum-group elements in pentlandite from the Bushveld Complex.
680 South Africa. *Miner Deposita*, 50, 41-54.
- 681 Johnson, J.W., Oelkers, E.H. and Helgeson, H.C. (1992) SUPCRT92: a software
682 package for calculating the standard molal thermodynamic properties of
683 minerals, gases, aqueous species, and reactions from 1 to 5000 bar and 0 to
684 1000 °C. *Computational Geosciences*, 18, 899–947
- 685 Klein, F. and Bach, W. (2009) Fe–Ni–Co–O–S phase relations in peridotite–seawater
686 interactions. *Journal of Petrology*, 50, 37–59.
- 687 Leblanc, M. (1991) Platinum-group elements and gold in ophiolitic complexes:
688 distribution and fractionation from mantle to oceanic floor[C]//Ophiolite
689 Genesis and Evolution of the Oceanic Lithosphere: Proceedings of the
690 Ophiolite Conference, held in Muscat, Oman. Springer Netherlands, 231-260.
- 691 Legendre, O. and Auge, T. (1986) Mineralogy of platinum-group mineral inclusion
692 in chromitites from different ophiolitic complexes. In: M.J. Gallagher, R.A. Ixer,
693 C.R. Neary and H.M. Prichard (Editors), *Metallogeny of Mafic and Ultramafic
694 Rocks*. Inst. Min. Metall., London, pp.361-372.
- 695 Li, W.X., Zhao, Z.D., Zhu, D.C., Dong, G.C. Zhou, S., Mo, X.X., Depaolo, D. and Dilek, Y.
696 (2012) Geochemical discrimination of tectonic environments of the Yalung
697 Zangbo ophiolite in southern Tibet. *Acta Petrol. Sinica*, 28(5), 1663–1673 (in
698 Chinese with English abstract).
- 699 Li, J., Kornprobst, J., Vielzeuf, D. and Fabri`es, J. (1995) An improved experimental
700 calibration of the olivine-spinel geothermometer. *Chinese Journal of
701 Geochemistry*, 14 (1), 68–77.

- 702 Liu, C. Z., Snow, J. E., Hellebrand, E., Brüggemann, G., von der Handt, A., Büchl, A., and
703 Hofmann, A. W. (2008). Ancient, highly heterogeneous mantle beneath Gakkel
704 ridge, Arctic Ocean. *Nature*, 452, 311–316.
- 705 Liu, J., Pearson, D. G., Shu, Q., Sigurdsson, H., Thomassot, E., and Alard, O. (2020).
706 Dating post-Archean lithospheric mantle: Insights from Re-Os and Lu-Hf
707 isotopic systematics of the Cameroon Volcanic Line peridotites. *Geochimica et*
708 *Cosmochimica Acta*, 278, 177–198.
- 709 Liu, J., Rudnick, R. L., Walker, R. J., Gao, S., Wu, F., and Piccoli, P. M. (2010). Processes
710 controlling highly siderophile element fractionations in xenolithic peridotites
711 and their influence on Os isotopes. *Earth & Planetary Science Letters*, 297(1–
712 2), 287–297.
- 713 Liu, Y.S., Hu, Z.C., Gao, S., Günther, D., Xu, J., Gao, C.G. and Chen, H.H. (2008) In situ
714 analysis of major and trace elements of anhydrous minerals by LA-ICP-MS
715 without applying an internal standard. *Chemical Geology*, 257(1-2), 34–43.
- 716 Lorand, J.-P., Alard, O., Godard, M. (2009). Platinum-group element signature of the
717 primitive mantle rejuvenated by melt-rock reactions: Evidence from Sumail
718 peridotites (Oman Ophiolite). *Terra Nova*, 21(1), 35–40.
- 719 Luguet, A. and Reisberg, L. (2016) Highly siderophile element and 187Os
720 signatures in non-cratonic basalt-hosted peridotite xenoliths: Unravelling
721 the origin and evolution of the post-Archean lithospheric mantle. *Reviews in*
722 *Mineralogy and Geochemistry*, 2016, 81(1): 305-367.
- 723 Luguet, A., Shirey, S. B., Lorand, J.-P., Horan, M. F., & Carlson, R. W. (2007). Residual
724 platinum-group minerals from highly depleted harzburgites of the Lherz
725 massif (France) and their role in HSE fractionation of the mantle. *Geochimica*
726 *et Cosmochimica Acta*, 71(12), 3082–3097
- 727 Maier, W.D., Barnes, S.J. and Groves, D.I. (2013) The Bushveld Complex, South
728 Africa: formation of platinum–palladium, chrome- and vanadium-rich layers
729 via hydrodynamic sorting of a mobilized cumulate slurry in a large, relatively
730 slowly cooling, subsiding magma chamber. *Mineralium Deposita*, 48, 1-56.

- 731 Malpas, J., Zhou, M.F., Robinson, P.T. and Reynolds, P. (2003) Geochemical and
732 geochronological constraints on the origin and emplacement of the Yarlung-
733 Zangbo ophiolites, Southern Tibet[C] // Dilek Y, Robinson P T eds, Ophiolites
734 Through Earth History. Geological Society, London, Special Publications, 218,
735 191–206
- 736 Matveev, S. and Ballhaus, C. (2002) Role of water in the origin of podiform
737 chromitites deposits. *Earth & Planetary Science Letters*, 235–243.
- 738 McDonough, W.F. and Sun, S.S. (1995) The composition of the Earth. *Chemical*
739 *Geology*, 120(3), 223–254.
- 740 McGowan N M, Griffin W L, González-Jiménez J M, et al. (2015) Tibetan chromitites:
741 Excavating the slab graveyard. *Geology*, 43(2), 179–182.
- 742 Meisel T., Walker R. J., Irving A. J. and Lorand J. P. (2001) Osmium isotopic
743 compositions of mantle xenoliths: a global perspective. *Geochimica et*
744 *Cosmochimica Acta*, 65, 1311–1323.
- 745 Melcher, F. (2000) Base metal - platinum-group element sulfides from the Urals
746 and the eastern Alps: Characterization and significance for mineral
747 systematics. *Mineralogy and Petrology*, 68(1–3), 177–211.
- 748 Melcher, F. and Meisel, T. (2004) A metamorphosed Early Cambrian crust–mantle
749 transition in the Eastern Alps, Austria. *Journal of Petrology*, 45, 1689–1723.
- 750 Melcher, F., Grum, W. and Simon, G. (1997) Petrogenesis of the ophiolitic giant
751 chromite deposits of Kempirsai, Kazakhstan: A study of solid and fluid
752 inclusions in chromite. *Journal of Petrology*, 38, 1419–1458.
- 753 Mondal, S. K. and Mathez, E. A. (2007) Origin of the UG2 chromitite layer, Bushveld
754 Complex. *Journal of Petrology*, 48(3), 495–510.
- 755 Naldrett, A.J. and Duke, J.M. (1980) Pt metals in magmatic sulfide ores. *Science*,
756 208, 1417–1424.
- 757 O'Driscoll, B., Day, J. M. D., Walker, R. J., Daly, J. S., McDonough, W. F. and Piccoli, P.
758 M. (2012). Chemical heterogeneity in the upper mantle recorded by
759 peridotites and chromitites from the Shetland Ophiolite Complex, Scotland.

- 760 Earth and Planetary Science Letters, 333–334, 226–237.
- 761 O'Driscoll, B., Walker, R. J., Clay, P. L., Day, J. M. D., Ash, R. D. and Daly, J. S. (2018).
762 Length-scales of chemical and isotopic heterogeneity in the mantle section of
763 the Shetland Ophiolite Complex, Scotland. Earth and Planetary Science
764 Letters, 488, 144–154.
- 765 O'Driscoll, B., Walker, R. J., Day, J. M. D., Ash, R. D. and Daly, J. S. (2015). Generations
766 of melt extraction, melt-rock interaction and high-temperature
767 metasomatism preserved in peridotites of the ~497 Ma Leka Ophiolite
768 Complex, Norway. Journal of Petrology, 56(9), 1797–1828.
- 769 Parkinson, I. J., Hawkesworth, C.J. and Cohen, A.S. (1998) Ancient mantle in a
770 modern arc: Osmium isotopes in Izu-Bonin-Mariana forearc peridotites.
771 Science, 281(5385), 2011–2013.
- 772 Pearson, D.G., Irvine, G.J., Ionov, D.A., Boyd, F.R. and Dreibus, G.E. (2004) Re–Os
773 isotope systematics and platinum group element fractionation during mantle
774 melt extraction: a study of massif and xenolith peridotite suites. Chemical
775 Geology, 208, 29–59.
- 776 Prelević, D., Brüggmann, G., Barth, M., Božović, M., Cvetković, V., Foley, S. F., and
777 Maksimović, Z. (2015). Os-isotope constraints on the dynamics of orogenic
778 mantle: The case of the Central Balkans. Gondwana Research, 27(4), 1560–
779 1573
- 780 Prichard, H.M., Sa, J.H.S. and Fisher, P.C. (2001) Platinum-group mineral
781 assemblages and chromite composition in the altered and deformed Bacuri
782 complex, Amapa, northeastern Brazil. Canadian Mineralogist, 39, 377–396
- 783 Proenza, J.A., Zaccarini, F., Escayola, M., Cábana, C., Shalamuk, A. and Garuti, G.
784 (2008) Composition and textures of chromite and platinum-group minerals
785 in chromitites of the western ophiolitic belt from Córdoba Pampeans Ranges,
786 Argentine. Ore Geology Reviews, 33, 32–48.
- 787 Rampone, E., Hoffman, A. W., Piccardo, G. B., Vannucci, R., Bottazzi, P., & Ottolini, L.
788 (1995). Petrology, mineral and isotope geochemistry of the external liguride

- 789 peridotites (Northern Apennines, Italy). *Journal of Petrology*, 36(1), 81–105.
- 790 Robinson, P.T., Bai, W.J., Malpas, J., et al. (2004) Ultra-high pressure minerals in the
791 Luobusa ophiolite, Tibet and their tectonic implications. *Aspects of the*
792 *Tectonic Evolution of China*. Geological Society, London, Special Publications,
793 226, 247–271.
- 794 Robinson, P.T., Trumbull, R.B., Schmitt, A., Yang, J.S., Li, J. W., Zhou, M.F., Erzinger, J.,
795 Dare, S. and Xiong, F.H. (2015) The origin and significance of crustal minerals
796 in ophiolitic chromitites and peridotites. *Gondwana Research*, 27, 486-506.
- 797 Rollinson, H. (2008) The geochemistry of mantle chromitites from the northern
798 part of the Oman ophiolite: inferred parental melt compositions.
799 *Contributions to Mineralogy and Petrology* 156, 273–288.
- 800 Rui, H.C., Yang, J.S., Llanes Castro, A.I., Zheng, J.P., Lian, D.Y., Wu, W.W. and Valdes
801 Marino, Y. (2022) Ti-poor high-Al chromitites of the Moa-Baracoa ophiolitic
802 massif (eastern Cuba) formed in a nascent forearc mantle. *Ore Geology*
803 *Reviews*, 144, 104847.
- 804 Scott, J. M., Liu, J., Pearson, D. G., Harris, G. A., Czertowicz, T. A., Woodland, S. J., et al.
805 (2019). Continent stabilization by lateral accretion of subduction zone-
806 processed depleted mantle residues; insights from Zealandia. *Earth and*
807 *Planetary Science Letters*, 507, 175–186.
- 808 Shi, R.D., Alard, O., Zhi, X.C., et al. (2007) Multiple events in the Neo-Tethyan oceanic
809 upper mantle: evidence from Ru–Os–Ir alloys in the Luobusa and Dongqiao
810 ophiolitic podiform chromitites, Tibet. *Earth & Planetary Science Letters*, 26,
811 33–48.
- 812 Stockman, H.W. and Hlava, P.F. (1984) Platinum-group minerals in Alpine
813 chromitites from southwestern Orogen. *Economic Geology*, 79(3), 491–508.
- 814 Su, B., Chen, C., Xiao, Y., Robinson, P.T., Liu, X., Wang, J., Uysal, I., Bai, Y. and Sun, Y.
815 (2021a) The Critical Role of Fluid-Mediated Diffusion in Anomalous Fe-Mg-O
816 Isotope Fractionations in Ultramafic Rocks of Ophiolites. *Journal of*
817 *Geophysical Research: Solid Earth*, 126(4): e2020JB020632.

- 818 Su, B., Robinson, P.T., Chen, C., Xiao, Y., et al. (2020) The occurrence, origin and fate
819 of water in chromitites in ophiolites. *American Mineralogist*, 105, 894–903.
- 820 Su, B.X., Liu, X., Robinson, P.T., et al. (2021b) A new model for chromitite formation
821 in ophiolite: Fluid immiscibility. *Science China Earth Sciences*, 64, 200.
- 822 Sun, Y. and Sun, M. (2005) Nickel sulfide fire assay improved for pre-concentration
823 of platinum group elements in geological samples: a practical means of ultra-
824 trace analysis combined with inductively coupled plasma-mass spectrometry.
825 *Analyst* 130, 664–669.
- 826 Sun, Y., Guan, K. and Du, A. (1998a) Determination of platinum group elements by
827 ICP-MS with nickel sulfide fire assay collection and tellurium coprecipitation.
828 *ICP Information Newsletter* 24, 114–115.
- 829 Sun, Y., Guan, X. and Du, A. (1998b) Determination of platinum group elements by
830 inductively coupled plasma-mass spectrometry combined with nickel sulfide
831 fire assay and tellurium coprecipitation. *Spectrochimica Acta Part B: Atomic*
832 *Spectroscopy* 53, 1463–1467.
- 833 Tsoupas, G., Economou-Eliopoulos, M. (2021) Transformation of PGM in supra
834 subduction zones: Geochemical and mineralogical constraints from the Veria
835 (Greece) podiform chromitites. *Geoscience Frontiers*, 12(2): 827–842.
- 836 Uçurum, A., Koptagel, O. and Lechler, P.J. (2006) Main-component geochemistry
837 and platinum-group element potential of Turkish chromite deposits, with
838 emphasis on the Muğla area. *International Geology Review* 48, 241–254
- 839 Ullah, Z., Khan, A., Faisal, S., Zafar, T., Li, H. and Farhan, M. (2022) Petrogenesis of
840 peridotites in the Dargai Complex ophiolite, Indus Suture Zone, Northern
841 Pakistan: Implications for two stages of melting, depletion, and enrichment of
842 the Neo-Tethyan mantle. *Lithos*, 426-427, 106798
- 843 Ullah, Z., Li, J.W., Robinson, P.T., Wu, W.W., Khan, A., Dac, N.X. and Adam, M. M.A.
844 (2020) Mineralogy and geochemistry of peridotites and chromitites in the
845 Jijal Complex ophiolite along the Main Mantle Thrust (MMT or Indus Suture
846 Zone) North Pakistan. *Lithos*, 366-367, 105566

- 847 Uysal, I., Akmaz, R.M., Kapsiotis, A., et al. (2015) Genesis and geodynamic
848 significance of chromitites from the Orhaneli and Harmanck ophiolites (Bursa,
849 NW Turkey) as evidenced by mineralogical and compositional data. *Ore
850 Geology Reviews*, 65, 26–41.
- 851 Uysal, I., Tarkian, M., Sadiklar, M.B. et al. (2007) Platinum-group-element
852 geochemistry and mineralogy of ophiolitic chromites from the Kop Mountains,
853 NE Turkey. *The Canadian Mineralogist*, 45, 355–377.
- 854 Uysal, İ., Tarkian, M., Sadiklar, M.B., Zaccarini, F. et al. (2009) Petrology of Al- and
855 Cr-rich ophiolitic chromitites from the Muğla, SW Turkey: implications from
856 composition of chromite, solid inclusions of platinum-group mineral, silicate,
857 and base-metal mineral, and Os-isotope geochemistry. *Contributions to
858 Mineralogy and Petrology*, 158(5), 659–674.
- 859 Uysal, I., Ersoy, E. Y., Karslı, O., Dilek, Y., Sadiklar, M. B., Ottley, C. J., et al. (2012).
860 Coexistence of abyssal and ultra-depleted SSZ type mantle peridotites in a
861 Neo-Tethyan Ophiolite in SW Turkey: Constraints from mineral composition,
862 whole-rock geochemistry (major-trace-REE-PGE), and Re-Os isotope
863 systematics. *Lithos*, 132–133, 50–69.
- 864 Wang, X.B., Bao, P.S., Deng, W.M., et al. (1987) Tibet ophiolite. Beijing: Geological
865 Publishing House, 1 - 336 (in Chinese with English abstract).
- 866 Wang, X.B., Zhou, X. and Hao, Z.G. (2010) Some opinions on further exploration for
867 chromite deposits in the Luobusa area, Tibet, China. *Geological Bulletin of
868 China* 29, 105–114 (in Chinese with English abstract).
- 869 White, R. W. and Powell, R. (2001) On the interpretation of retrograde reaction
870 textures in granulite facies rocks, *Journal of Metamorphic Geology*, 29, 131–
871 149.
- 872 Wilson, S. A., Ridley, W.I. and Koenig, A.E. (2002) Development of sulfide
873 calibration standards for the laser ablation inductively-coupled plasma mass
874 spectrometry technique. *Journal of Analytical Atomic Spectrometry*, 17, 406–
875 409.

- 876 Wirth, R., Reid, D. and Schreiber, A. (2013) Nanometer-sized platinum-group
877 minerals (PGM) in base metal sulfides: new evidence for an orthomagmatic
878 origin of the Merensky reef PGE ore deposit. Bushveld Complex. South Africa.
879 Canadian Mineralogist, 51, 143–155.
- 880 Wise, A.S. and Watters, R.L. (2012) Certificate of Analysis, Standard Reference
881 Material 610, National Institute of Standards and Technology,
882 <http://www.nist.gov/srm>.
- 883 Wohlgemuth-Ueberwasser, C.C., Ballhaus, C., Berndt, J., Stotter nee Paliulionyte, V.
884 and Meisel, T. (2007) Synthesis of PGE sulfide standards for laser ablation
885 inductively coupled plasma mass spectrometry (LA-ICP-MS). Contributions to
886 Mineralogy and Petrology, 154(5), 607–617.
- 887 Wolf, R.E. and Wilson, S.A. (2007) USGS Reference Materials Program: USGS Fact
888 Sheet 2007-3056, 1–4.
- 889 Xiong, F.H., Xu, X.Z., Zoheir, B., Lenaz, D. and Yang, J.S. (2022b) Genesis and
890 evolution of the Köycegiz ophiolite (SW Turkey): Mineralogical and
891 geochemical characteristics of associated podiform chromitite. Ore Geology
892 Reviews, 145, 104912.
- 893 Xiong, F.H., Yang, J.S., Robinson, P.T., et al. (2017) High-Al and high-Cr podiform
894 chromitites from the western Yarlung-Zangbo suture zone, Tibet:
895 Implications from mineralogy and geochemistry of chromian spinel, and
896 platinum-group elements. Ore Geology Reviews, 80, 1020–1041.
- 897 Xiong, F.H., Yang, J.S., Robinson, P.T., Xu, X.Z., Liu, Z., Li, Y., Li, J.Y. and Chen, S.Y. (2015)
898 Origin of podiform chromitite, a new model based on the Luobusa ophiolite,
899 Tibet. Gondwana Research, 27, 525–542.
- 900 Xiong, F.H., Yang, J.S., Xu, X.Z., Kapsiotis, A., Hao, X.L. and Liu, Z. (2018)
901 Compositional and isotopic heterogeneities in the Neo-Tethyan upper mantle
902 recorded by coexisting Al-rich and Cr-rich chromitites in the Purang
903 peridotite massif, SW Tibet (China). Journal of Asian Earth Sciences, 159,
904 109–129.

- 905 Xiong, F.H., Zoheir, B., Robinson, P.T., Wirth, R., Xu, X.Z., Qiu, T. and Sun, Y. (2022a)
906 Microchemistry and magnesium isotope composition of the Purang ophiolitic
907 chromitites (SW Tibet): New genetic inferences. American Mineralogist,
908 doi.org/10.2138/am-2022-8392.
- 909 Xiong, F.H., Zoheir, B., Wirth, R., Milushi, I., Qiu, T. and Yang, J.S. (2021)
910 Mineralogical and isotope peculiarities of high-Cr chromitites: Implications
911 for a mantle convection genesis of the Bulqiza ophiolite. Lithos, 398–399,
912 106305.
- 913 Xiong, Q., Dai, H.K., Zheng, J.P., Griffin, W.L., Zheng, H.D., Wang, L. and O'Reilly, S.Y.
914 (2022) Vertical depletion of ophiolitic mantle reflects melt focusing and
915 interaction in sub-spreading-center asthenosphere. Nature Communications
916 13, 6956
- 917 Xu, X.Z., Yang, J.S., Chen, S.Y., Fang, Q.S., Bai, W.J. and Ba, D.Z. (2009) Unusual mantle
918 mineral group from chromitite orebody Cr-11 in Luobusa ophiolite of the
919 Yarlung–Zangbo suture zone, Tibet. Journal of Earth Sciences, 20:284–302.
- 920 Xu, X.Z., Yang, J.S., Guo, G.L. and Li, G.Y. (2011) Lithological research on the Purang
921 mantle peridotite in western Yarlung-Zangbo suture zone in Tibet. Acta
922 Petrologica Sinica, 27(11), 3179–3196 (in Chinese with English abstract).
- 923 Xu, X.Z., Yang, J.S., Robinson, P.T., Xiong, F.H., Ba, D.Z. and Guo, G.L. (2015) Origin of
924 ultrahigh pressure, highly reduced and crustal-type minerals from podiform
925 chromitite and mantle peridotite of the Luobusa ophiolite, Tibet. Gondwana
926 Research, 27, 686-700.
- 927 Xu, X.Z., Xiong, F.H., Basem, Z., Yan, J.Y., Zhang, B.Y., Gao, J. and Yang, J.S. (2023)
928 Genesis of Pyroxenite Veins in the Zedang Ophiolite, Southern Tibetan Plateau.
929 Acta Geologica Sinica - English Edition, 97, 707–726.
- 930 Xu, Y. and Liu, C.-Z. (2019). Subduction-induced fractionated highly siderophile
931 element patterns in forearc mantle. Minerals, 9, 339.
- 932 Xu, Y., Liu, J., Xiong, Q., Su, B.-X., Scott, J. M., Xu, B., et al. (2020). The complex life
933 cycle of oceanic lithosphere: A study of Yarlung-Zangbo ophiolitic peridotites,

- 934 Tibet. *Geochimica et Cosmochimica Acta*, 277, 175–191.
- 935 Xu, Y., Li, D.N., Li, D.X., Dong, G.C., Pearson, D.G., Liu, J.G. (2021). Modification of
936 Lithospheric Mantle by Melts/Fluids With Different Sulfur Fugacities During
937 the Wilson Cycle: Insights From Lesvos and Global Ophiolitic Peridotites.
938 *Journal of Geophysical Research: Solid Earth*, 126, e2021JB022445
- 939 Yao, J., Xu, J., Wu, C., Zhang, Z., Rosana, M.F., Li, X., Jin, Z. (2023). Origin of high-Cr
940 podiform chromitites from Kabaena Island, Southeast Sulawesi, Indonesia:
941 constraints from mineralogy and geochemistry. *International Geology Review*,
942 DOI:10.1080/00206814.2023.2167130
- 943 Yamamoto, S., Komiya, T., Hirose, K. and Maruyama, S. (2009) Coesite and
944 clinopyroxene exsolution lamellae in chromites: In-situ ultrahigh-pressure
945 evidence from podiform chromitites in the Luobusa ophiolite, southern Tibet.
946 *Lithos*, 109, 314–322.
- 947 Yang, J.S., Dobrzhinetskaya, L., Bai, W.J., Fang, Q.S., Robinson, P.T., Zhang, J. and
948 Green, H.W. (2007) Diamond-and coesite-bearing chromitites from the
949 Luobusa ophiolite, Tibet. *Geology*, 35, 875–878.
- 950 Yang, J.S., Robinson, P.T. and Dilek, Y. (2014) Diamonds in Ophiolites: a little –
951 known diamond occurrence. *Elements*, 10, 123–126.
- 952 Yang, J.S., Wu, W.W., Lian, D.Y. and Rui, H. (2021) Peridotites, chromitites and
953 diamonds in ophiolites. *Nature Reviews Earth & Environment*, 2(3), 198-212.
- 954 Zaccarini, F., Proenza, J.A., Ortega-Gutiérrez, F. and Garuti, G. (2005) Platinum
955 group minerals in ophiolitic chromitites from Tehuizingo (Acatlán complex,
956 southern Mexico): implications for post-magmatic modification. *Mineralogy
957 and Petrology*, 84(3), 147–168.
- 958 Zhang, P.F., Zhou, M.F., Robinson, P.T., et al. (2019) Evolution of nascent mantle
959 wedges during subduction initiation: Li-O isotopic evidence from the Luobusa
960 ophiolite, Tibet. *Geochimica et Cosmochimica Acta*, 245, 35–58.
- 961 Zhang, P. F., Zhou, M. F., Su, B. X., Uysal, I., Robinson, P. T., Avci, E. and He, Y. S. (2017)
962 Iron isotopic fractionation and origin of chromitites in the paleo-Moho

- 963 transition zone of the Kop ophiolite, NE Turkey. *Lithos*, 268, 65-75.
- 964 Zhang, P. F., Zhou, M. F., Malpas, J. and Robinson, P. T. (2020) Origin of high-Cr
965 chromite deposits in nascent mantle wedges: petrological and geochemical
966 constraints from the neo-Tethyan Luobusa ophiolite, Tibet *Ore Geology
967 Reviews*, 123, 103581.
- 968 Zhang, P. F., Zhou, M. F., Liu, Q. Y., Malpas, J., Yumul Jr, G. P. and Wang, C. Y. (2023)
969 Sluggish Slab Rollback at the Early Stage of Flux Melting During Subduction
970 Initiation: Li Isotopic Evidence From the Coto High-Al Chromite Deposit,
971 Zambales Ophiolite, Philippines. *Journal of Geophysical Research: Solid Earth*,
972 128(4), e2022JB025562.
- 973 Zhou, M.F. and Robinson, P.T. (1994) High-chromium and high-aluminum podiform
974 chromitites, western china: relationship to partial melting and melt/rock
975 interaction in the upper mantle. *International Geology Reviews*, 36, 678–686.
- 976 Zhou, M.F., Robinson, P.T., Malpas, J. and Li, Z. (1996) Podiform chromitites in the
977 Luobusa Ophiolite (southern Tibet); implications for melt–rock interaction
978 and chromite segregation in the upper mantle. *Journal of Petrology*, 37 (1), 3–
979 21.
- 980 Zhou, M.F., Robinson, P.T., Malpas, J., Edwards, S.J. and Qi, L. (2005) REE and PGE
981 geochemical constraints on the formation of dunites in the Luobusa ophiolite,
982 southern Tibet. *Journal of Petrology*, 46, 615–639.
- 983 Zhou, M.F., Robinson, P.T., Su, B.X., Gao, J.F., Li, J.W., Yang, J.S. and Malpas, J. (2014)
984 Compositions of chromite, associated minerals, and parental magmas of
985 podiform chromite deposits: The role of slab contamination of
986 asthenospheric melts in suprasubduction zone environments. *Gondwana
987 Research*, 26, 262–283.
- 988 Zhou, S., Mo, X.X., Mahoney, J.J., et al. (2002) Geochronology and Nd and Pb isotope
989 characteristics of gabbro dikes in the Luobusa ophiolite, Tibet. *Chinese
990 Science Bulletin*, 47, 143–146.
- 991 Zhu, Q. and Zhu, Y. (2019) Platinum-group minerals and Fe–Ni minerals in the

992 Sartohay podiform chromitite (west Junggar, China): Implications for T-pH-
993 fO_2 - fS_2 conditions during hydrothermal alteration. Ore Geology Reviews, 112,
994 103020.

995 **Figure captions**

- 996 Figure 1. Geological map of the Luobusa ophiolite, modified from Xiong et al.
997 (2015). Cumulate rocks include grabbros, wehrlite, and pyroxenite.
- 998 Figure 2. Field photographs illustrating the occurrence of chromitite in the
999 Luobusa ophiolite. (a) Disseminated chromitite in the dunite unit. (b)
1000 Disseminated chromite in dunite and small nodules of massive chromitite. (c)
1001 Well-developed nodular chromitite in contact with dunite containing thin
1002 layers of disseminated chromite. (d) Sharp contact between massive
1003 chromitite and dunite.
- 1004 Figure 3. Petrographic features of the BMS inclusions in the Luobusa chromitites.
1005 (a) Reflected light microphotograph of pyrite inclusions. (b)-(o)
1006 Backscattered electron (BSE) images of (b) Galena inclusion in chromite. (c)
1007 Millerite inclusion. (d) Awaruite inclusion. (e) Irregular millerite inclusions. (f)
1008 Pyrite intergrowth with millerite. (g) Amphibole inclusions in pentlandite. (h)
1009 Serpentine and Ni in NiS inclusion. (i) Chalcocite inclusion. (j)-(k) Millerite
1010 and serpentine intergrowths. (l) Millerite intergrown with clinopyroxene. (m)
1011 Quartz and chalcocite inclusions in pyrite. (n) Awaruite intergrown with
1012 millerite as inclusions in chromite. (o) Intergrown Co-Fe-Ni-S and millerite in
1013 chromite. Py = pyrite, Gn = galena, Mlr = millerite, Pn = pentlandite, Amp =
1014 amphibole, Serp = serpentine, Cc = chalcocite, Cpx = clinopyroxene, Qz =
1015 quartz, Awr = awaruite, Chr = chromite.
- 1016 Figure 4. BSE images of pyrite and other mineral inclusions in the Luobusa
1017 chromitites. Sh = schuetteite, Py = pyrite, Srp = serpentine, Sph = sphalerite,
1018 Tnt-Zn = tennantite-(Zn), Gn = galena, Ttr-Zn = tetrahedrite-(Zn).
- 1019 Figure 5. BSE images of different PGM inclusions and alloys in chromite from the
1020 Luobusa ophiolite. (a-c) PGM inclusions are dispersed as single-phase, (d-i)
1021 Polyphase hypidiomorphic and xenomorphic PGE alloys. In some examples,
1022 symplectite textures with microscopic multiphase (Fe-Ni, Ir-Fe)
1023 pseudostructures in Os-Ir, Os-Ir-As, Lrt, Os-Al, and Ir-Al matrices (d, e, f). Lrt
1024 = laurite, Chr = chromite.
- 1025 Figure 6. Triangular diagram illustrating the compositional variation of PGM and
1026 alloys in the Luobusa chromitite. (a) Classification of PGM in the Luobusa

1027 chromitites based on Ru, Os, etc., compared with data from Cabri (2002) and
1028 Bai et al. (2004). (b) Ternary diagram depicting the compositional variation
1029 of Fe–Ni–Pt alloys in the Luobusa chromitites in terms of Pt, Rh, Os – Ni, Co,
1030 Cu – Fe.

1031 Figure 7. Binary plots of pyrite trace element compositions. Measurements below
1032 the minimum detection limit were excluded.

1033 Figure 8. Chondrite-normalized (Naldrett and Duke 1980) PGE patterns for
1034 chromitite (a) and dunite (b) in the Luobusa ophiolite, compared with other
1035 podiform chromitites (data sources: Uysal et al. 2007; Rui et al. 2022).

1036 Figure 9. Plots of whole-rock compositions: (a) $(Pt/Ir)_N$ versus $(Pd/Ir)_N$; (b) $1/Os$
1037 versus Pd/Ir ; (c) $1/Os$ versus Os/Ir (based on Xu et al. 2020, 2021). The melt
1038 extraction curve was calculated using nonmodal fractional melting, assuming
1039 a primitive mantle source with 300 ppm S and extracted melts with a sulfur
1040 concentration of 1000 ppm. The primitive upper mantle (PUM) values of
1041 these ratios are from Meisel et al. (2001). The plot includes abyssal
1042 peridotites (Parkinson et al. 1998; Liu et al. 2008; Day et al. 2017; Xu and Liu
1043 2019; Scott et al. 2019), massif peridotites (data from Becker et al., 2006;
1044 Fischer-Gödde et al., 2011; Lorand et al., 2009; Luguet et al., 2007; Rampone
1045 et al., 1995; etc.), and forearc peridotites (SSZ; data from Haller et al., 2021;
1046 O'Driscoll et al., 2012, 2015, 2018; Prelević et al., 2015; Uysal et al., 2012; etc.).
1047 The high-Cr and high-Al chromitite data are from Rui et al. (2022).

1048 Figure 10. (a) Metal-sulfide equilibrium curves for Ru, Os, Ir, and Ni as a function
1049 of sulfur fugacity ($\log f_{S_2}$) and temperature (T) based on Stockman and Hlava
1050 (1984) and Garuti et al. (1990). (b) Oxygen fugacity (f_{O_2}) versus sulfur
1051 fugacity (f_{S_2}) diagram in the Fe–Ni–Cu–O–S system at 300 °C and 50 MPa,
1052 providing insights into the evolution of Fe–Ni minerals in the matrix of
1053 Luobusa chromitite (adapted from Zhu and Zhu 2019).

1054 Figure 11. Conceptual genetic model of the formation of PGM and BMS inclusions
1055 in the Luobusa chromitites. (a) Early-stage melt interaction with harzburgitic
1056 peridotite. (b) Accumulation of chromite spinel in layers or pockets and

1057 encapsulation of BMS, PGE-bearing sulfides, and PGM inclusions during
1058 chromite crystallization at high temperatures. (c) Serpentinization and melt
1059 percolation during subduction, leading to the appearance of amphibole and
1060 other hydrous minerals, alteration of PGE-bearing minerals and Ni-sulfides,
1061 and precipitation of pyrite, as well as Ag, Pb, Bi-sulfide phases. Ol = olivine,
1062 Opx = orthopyroxene, Spl = spinel, Pn = pentlandite, Lrt = laurite, Chr =
1063 chromite.

1064 **Supplementary Material**

1065 Fig. S1 Backscattered electron (BSE) images showing morphology, texture and
1066 mineral assemblage of the discovered PGM, BMS and silicates in Luobusa
1067 chromitites.

1068 Fig. S2 Mapping of millerite intergrown with serpentine in chromite (Fig. 3j).

1069 Fig. S3 Millerite intergrowth with serpentine in chromite (Fig. 3k).

1070 Fig. S4 Awaruite intergrowth with millerite in chromite (Fig. 3n).

1071 Fig. S5 Co-Fe-Ni-S intergrowths with millerite in chromite (Fig. 3o).

1072 Fig. S6 Millerite intergrowth with PGM in the chromite.

1073 Fig. S7 PGE-bearing alloys in chromite (Fig. 5f).

1074 Fig. S8 The thermodynamic context of crystallization conditions for melt-sulfide
1075 (after Uysal et al. 2015)

1076

1077 **Table captions:**

1078 **Table S1.** Representative compositions of sulfides in Luobusa chromitite (wt%).

1079 **Table S2.** Compositions of sulfide inclusions in the Luobusa chromitite (wt%).

1080 **Table S3.** Compositions of the PGM alloys in the Luobusa chromitite (wt%).

1081 **Table S4.** Compositions of PGM alloys in the Luobusa chromitite (wt%).

1082 **Table S5.** Compositions of Fe-Ni phases in the Luobusa chromitite (wt%).

1083 **Table S6.** Trace element analysis of pyrite in the Luobusa chromitite.

1084 **Table S7.** PGE contents of chromitites in the Luobusa ophiolite.

1085

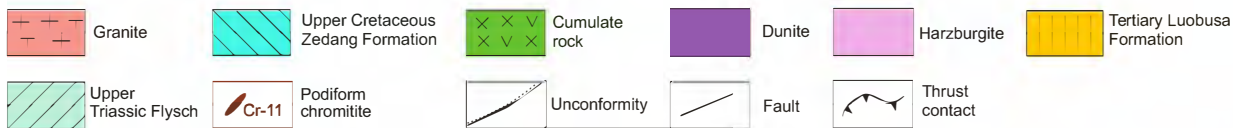
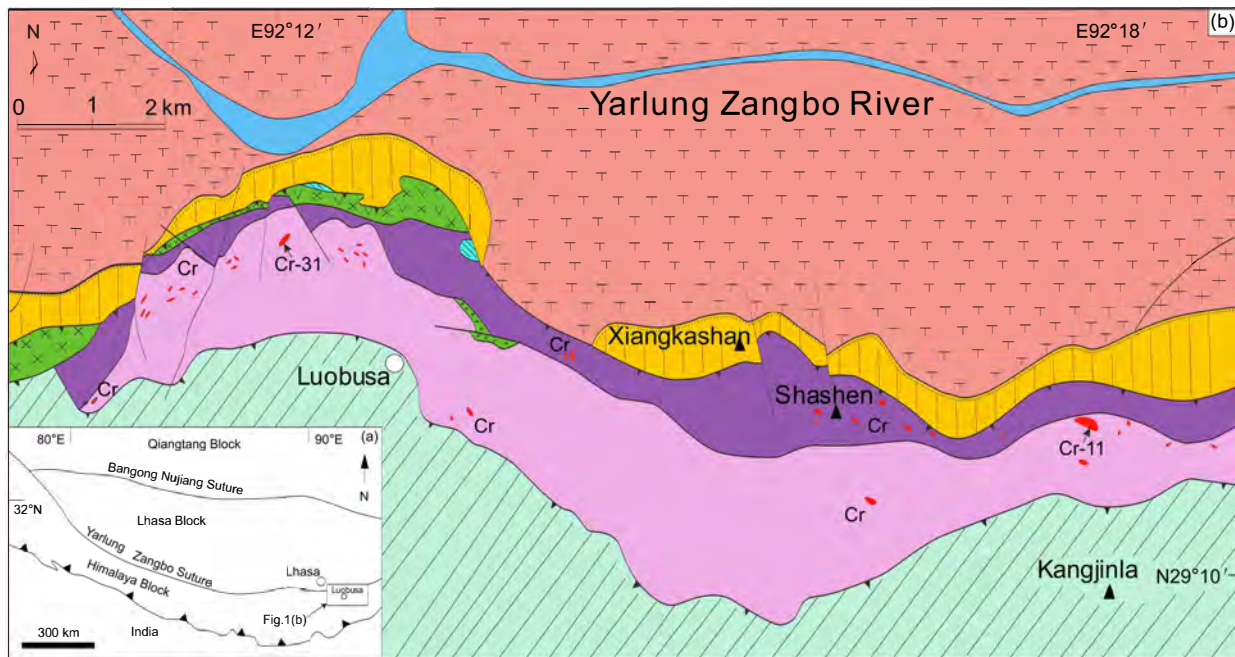


Figure 1

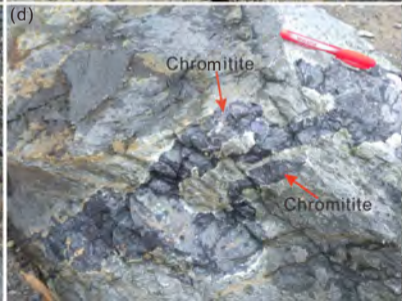
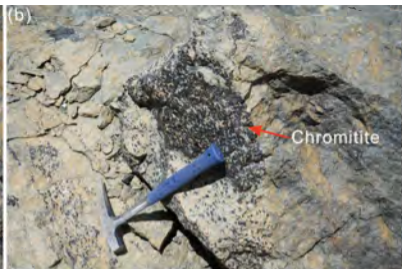
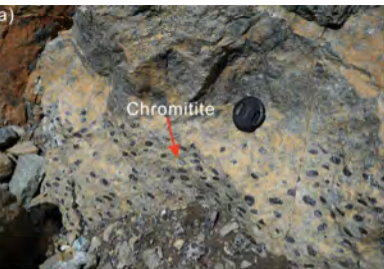


Figure 2

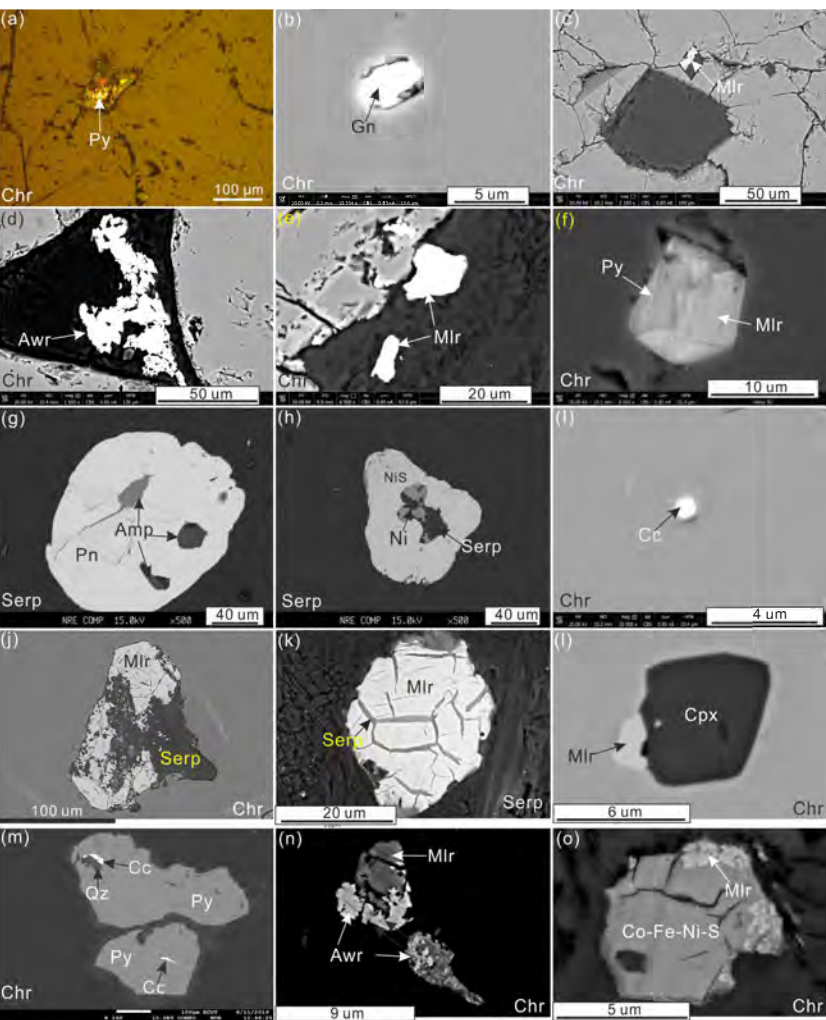


Figure 3

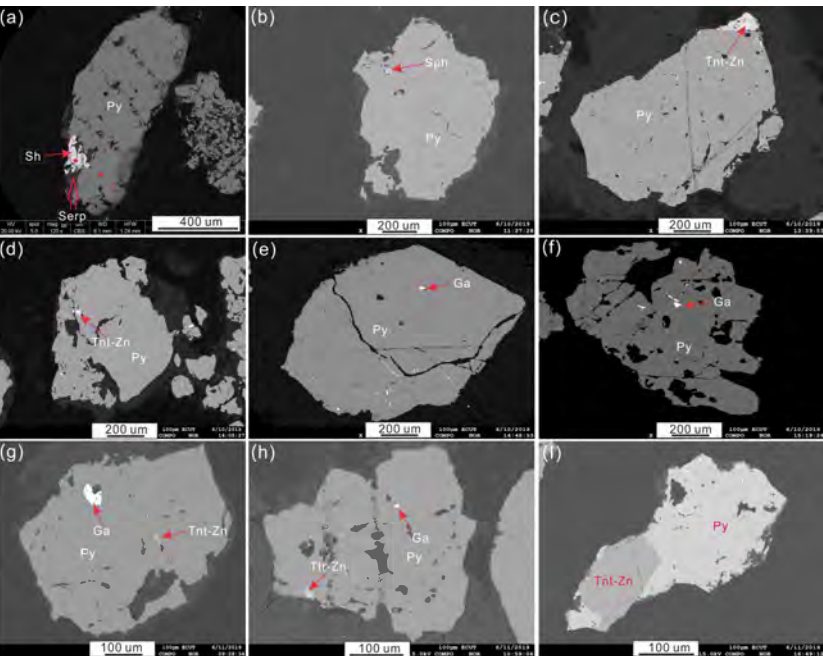


Figure 4

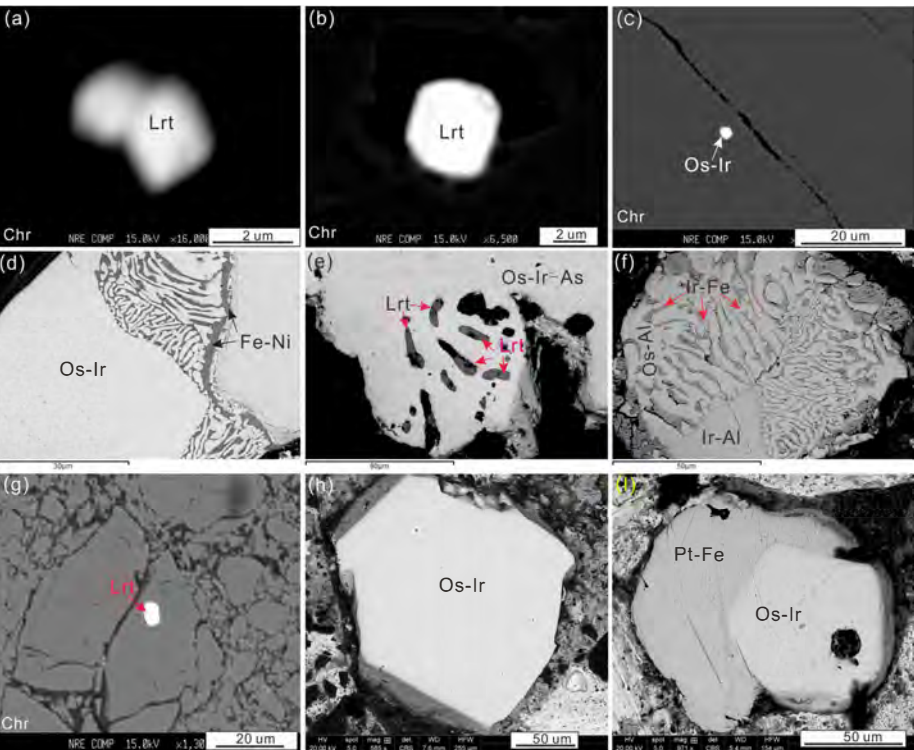


Figure 5

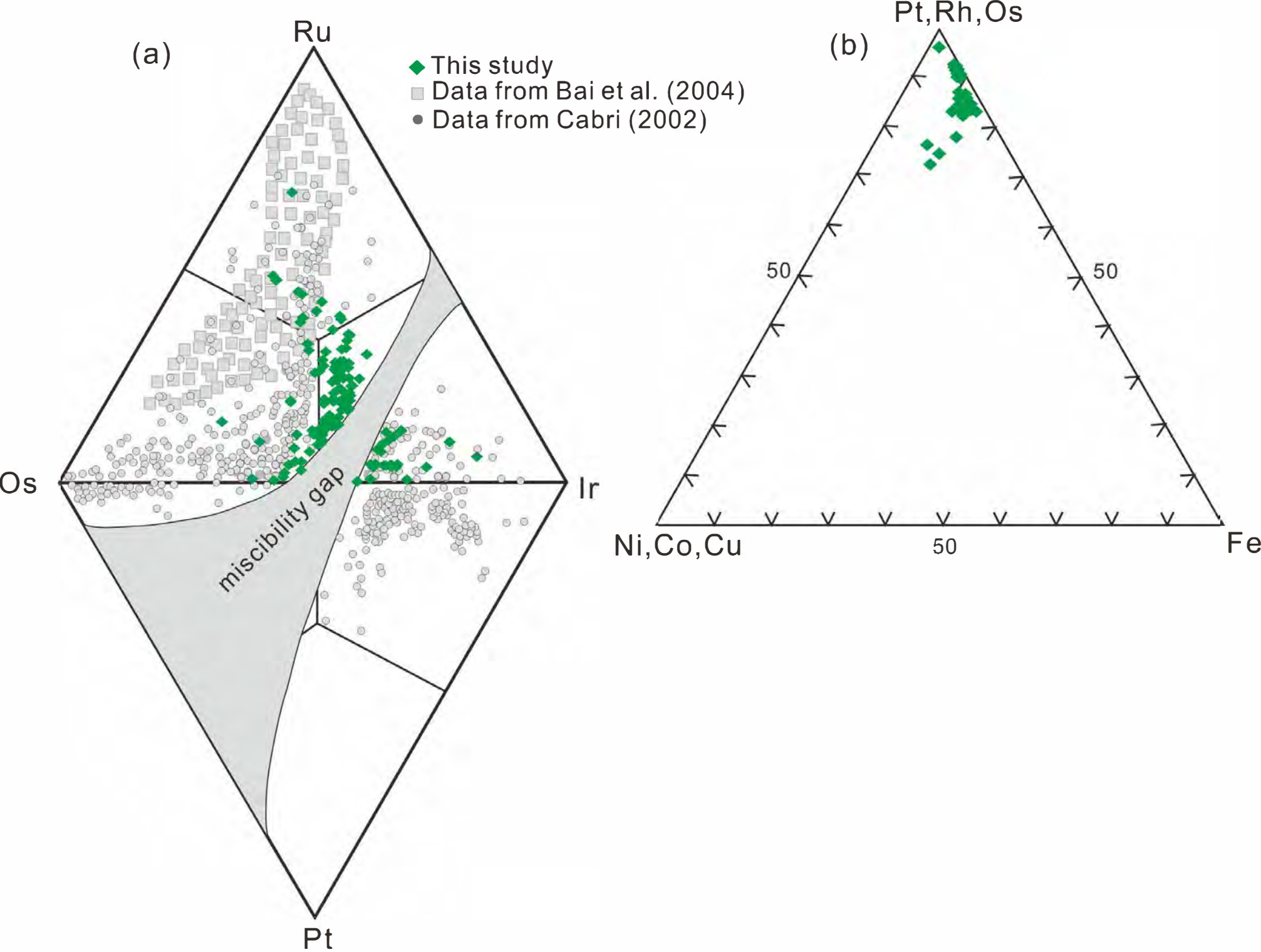


Figure 6

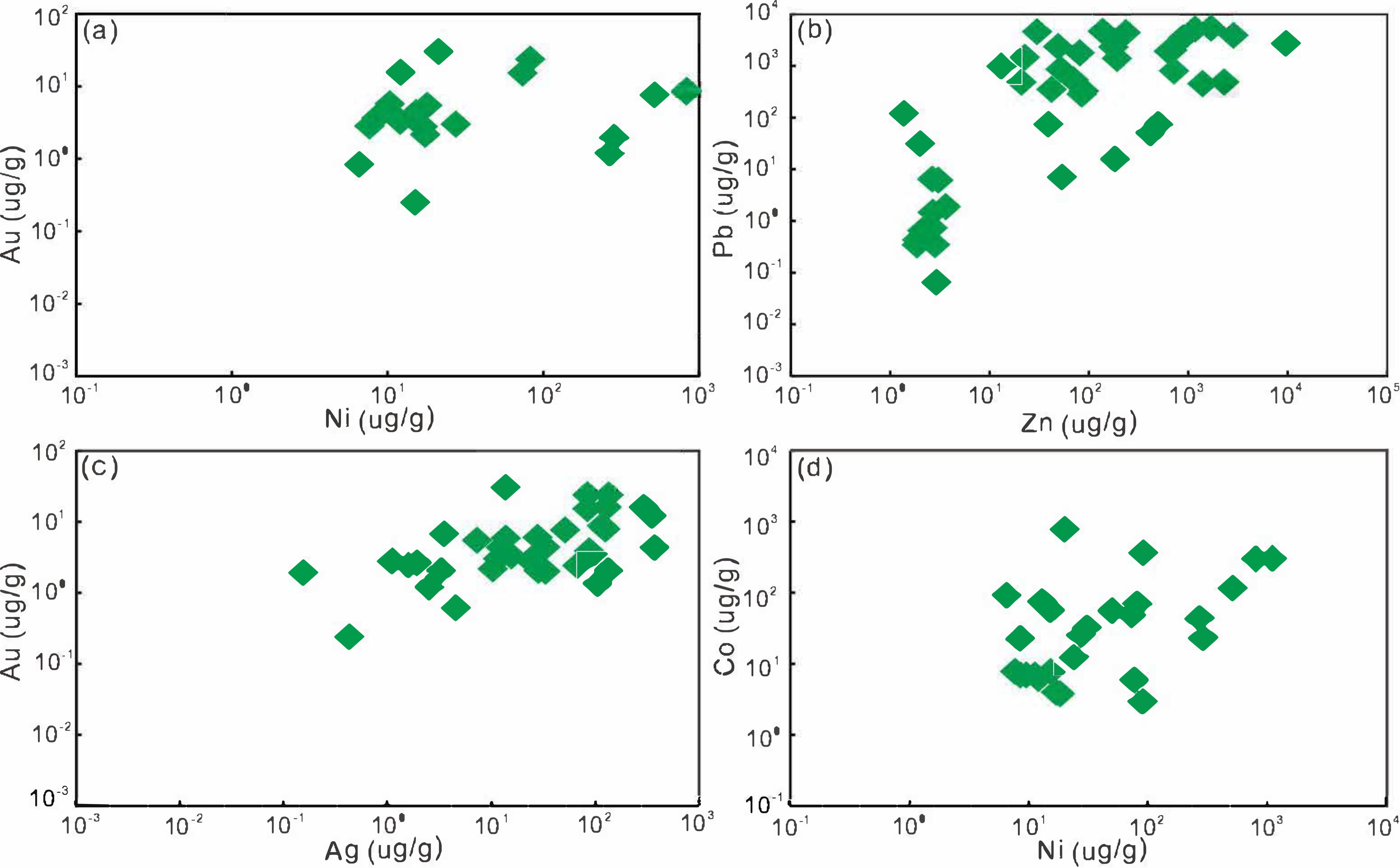


Figure 7

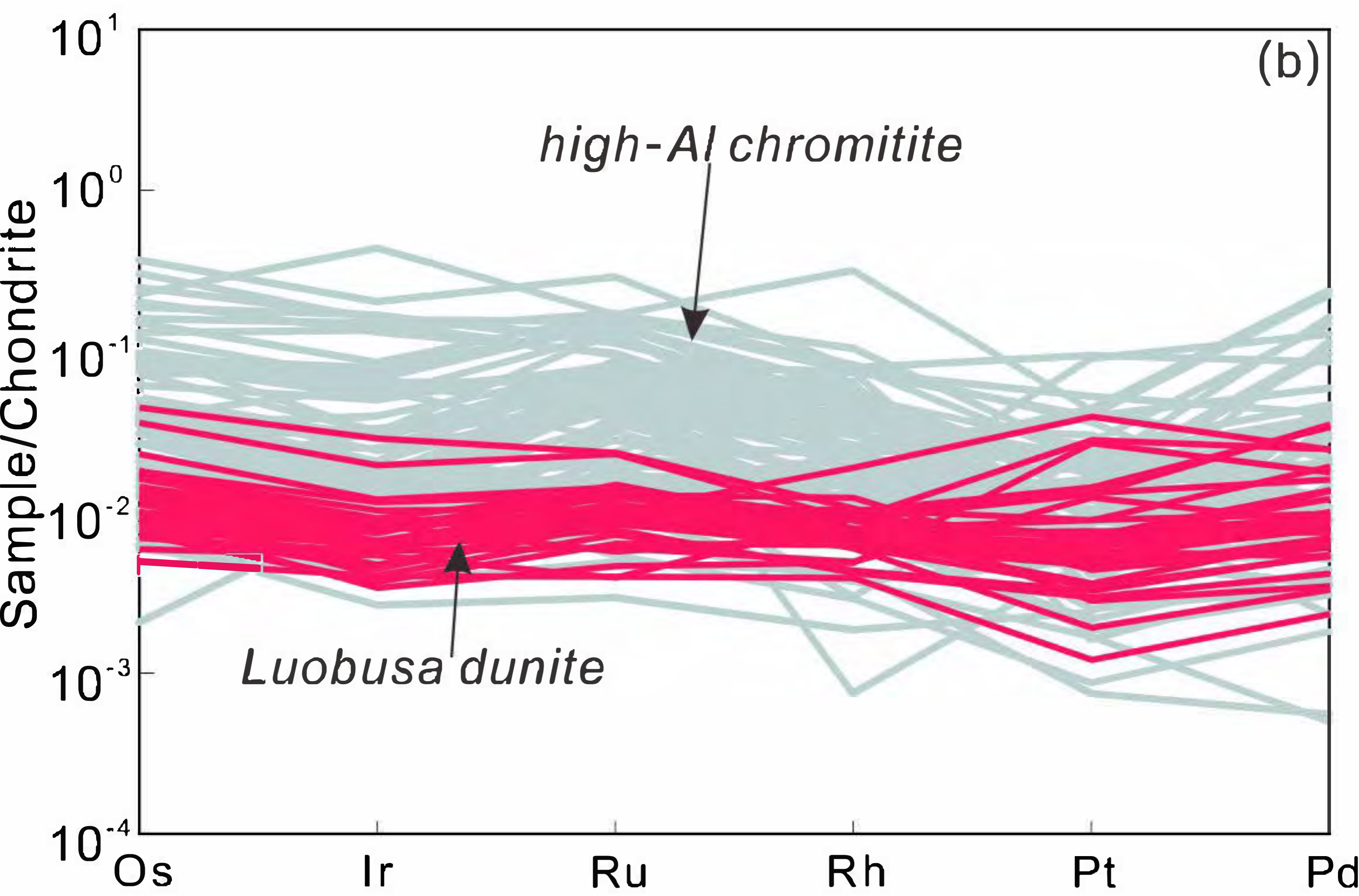
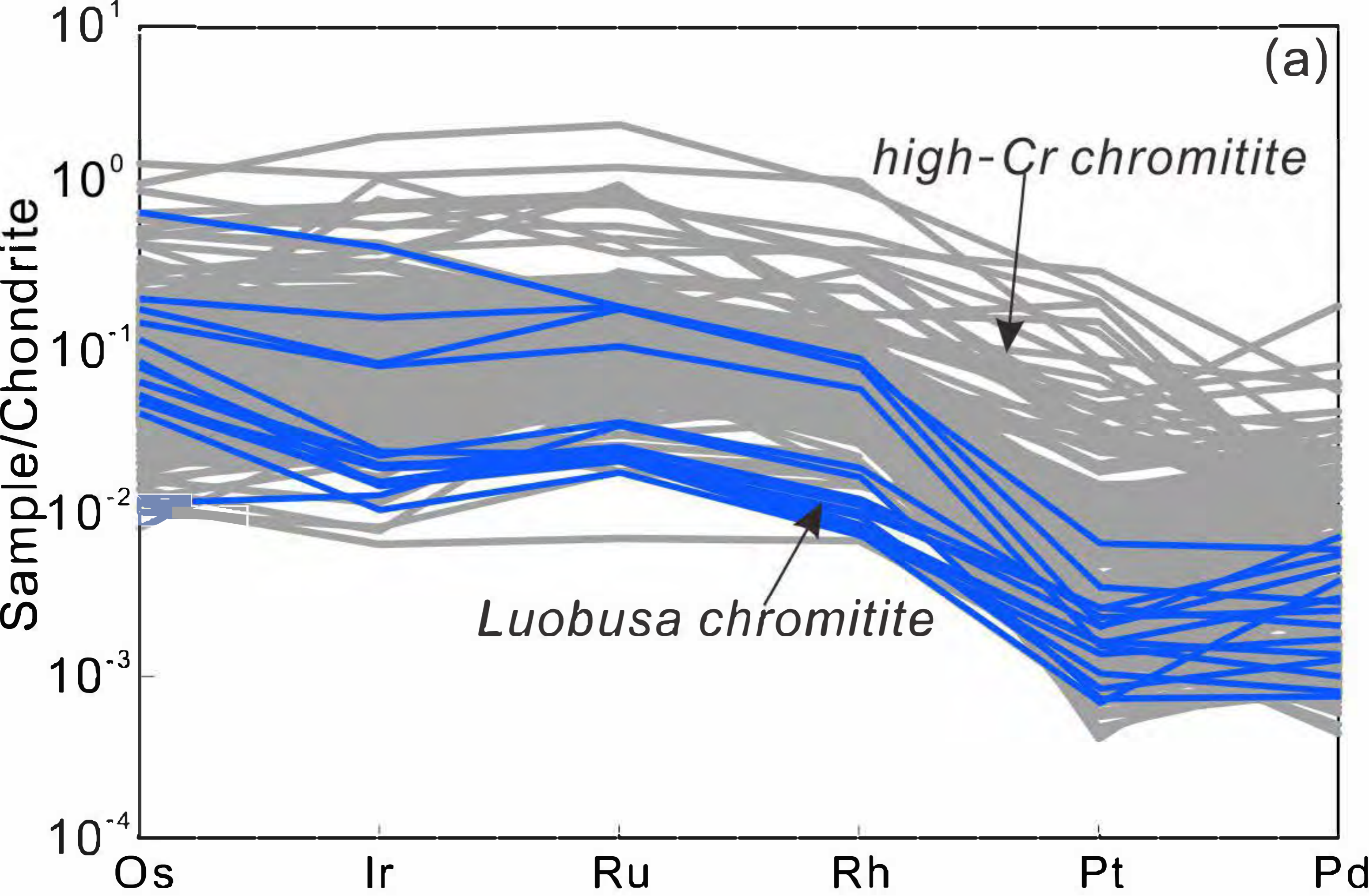


Figure 8

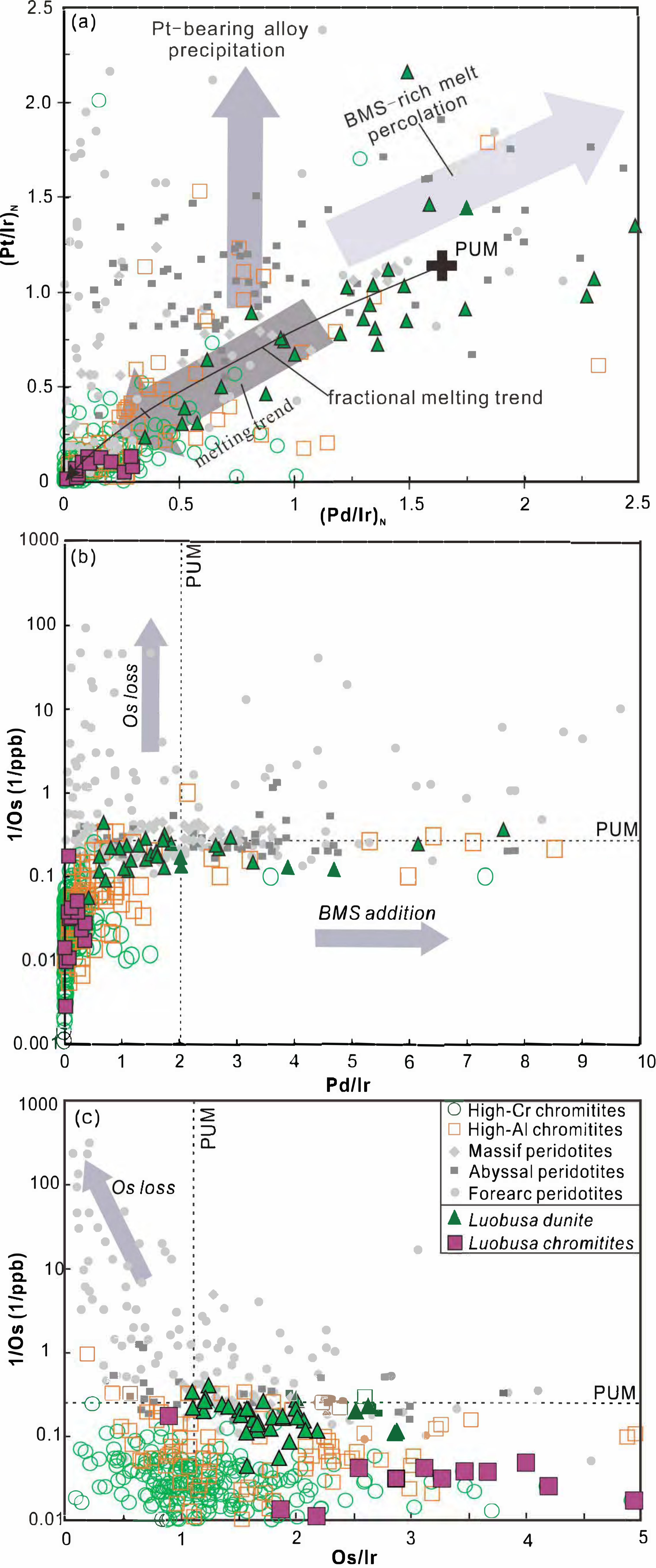


Figure 9

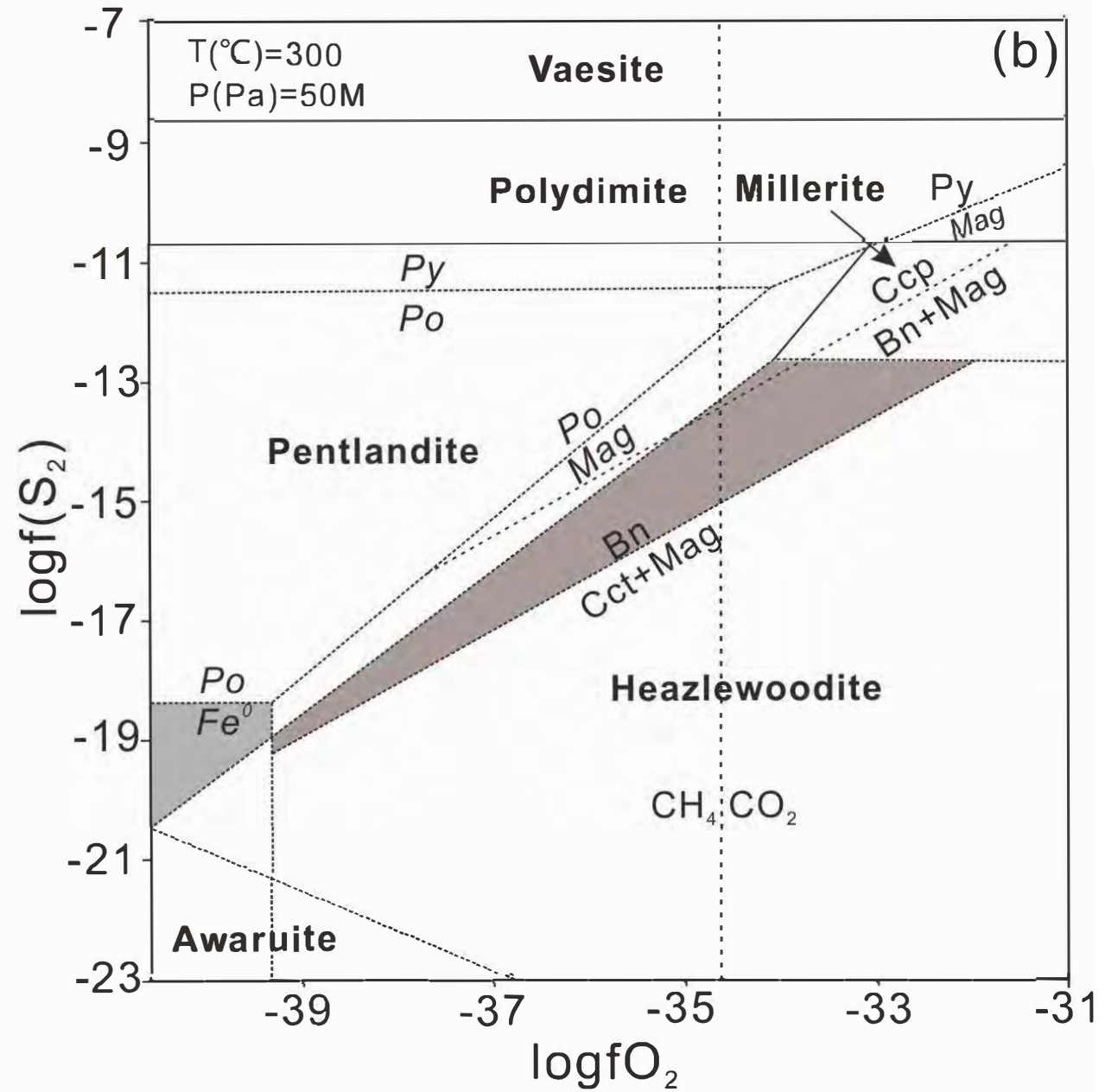
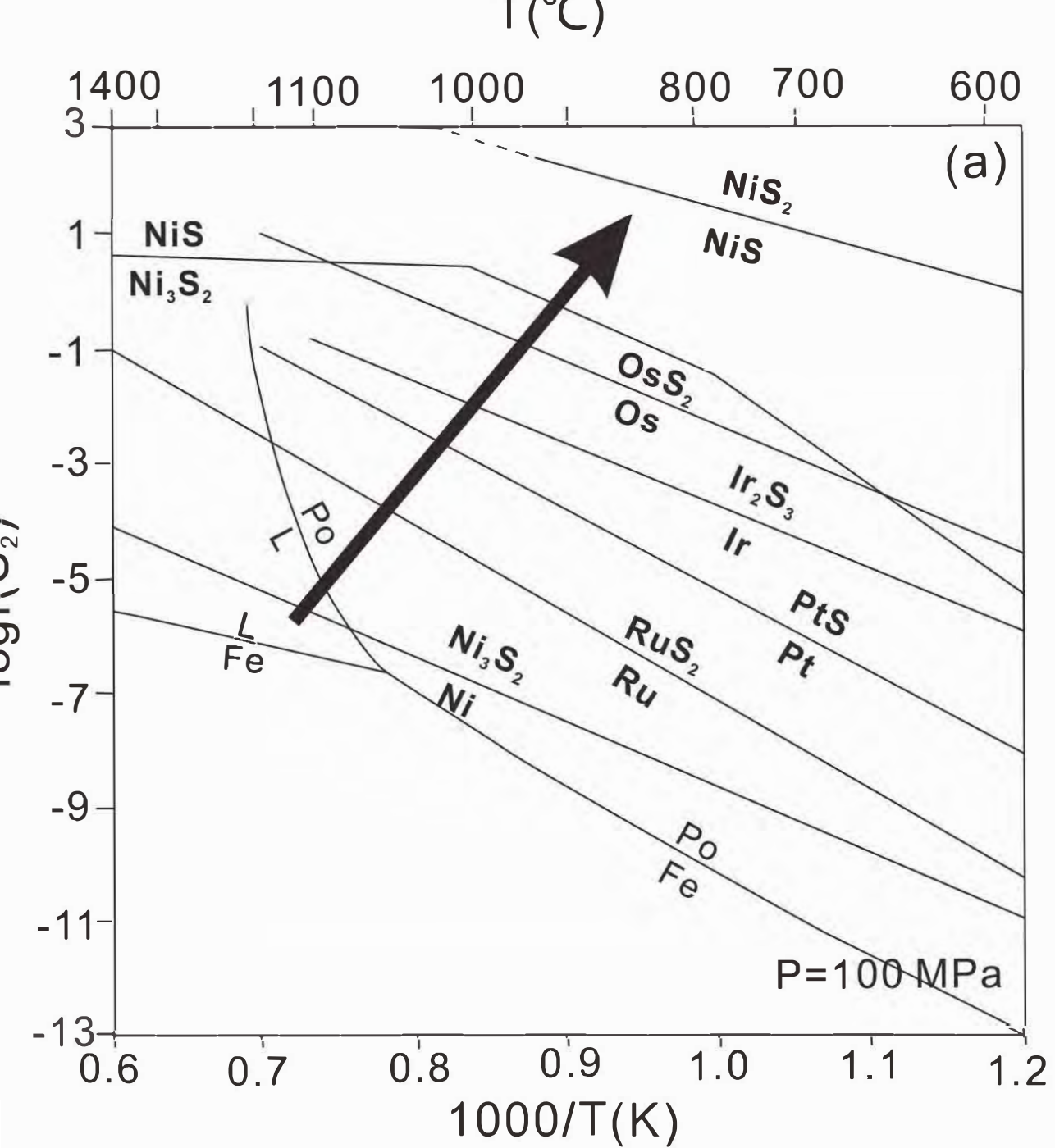


Figure 10

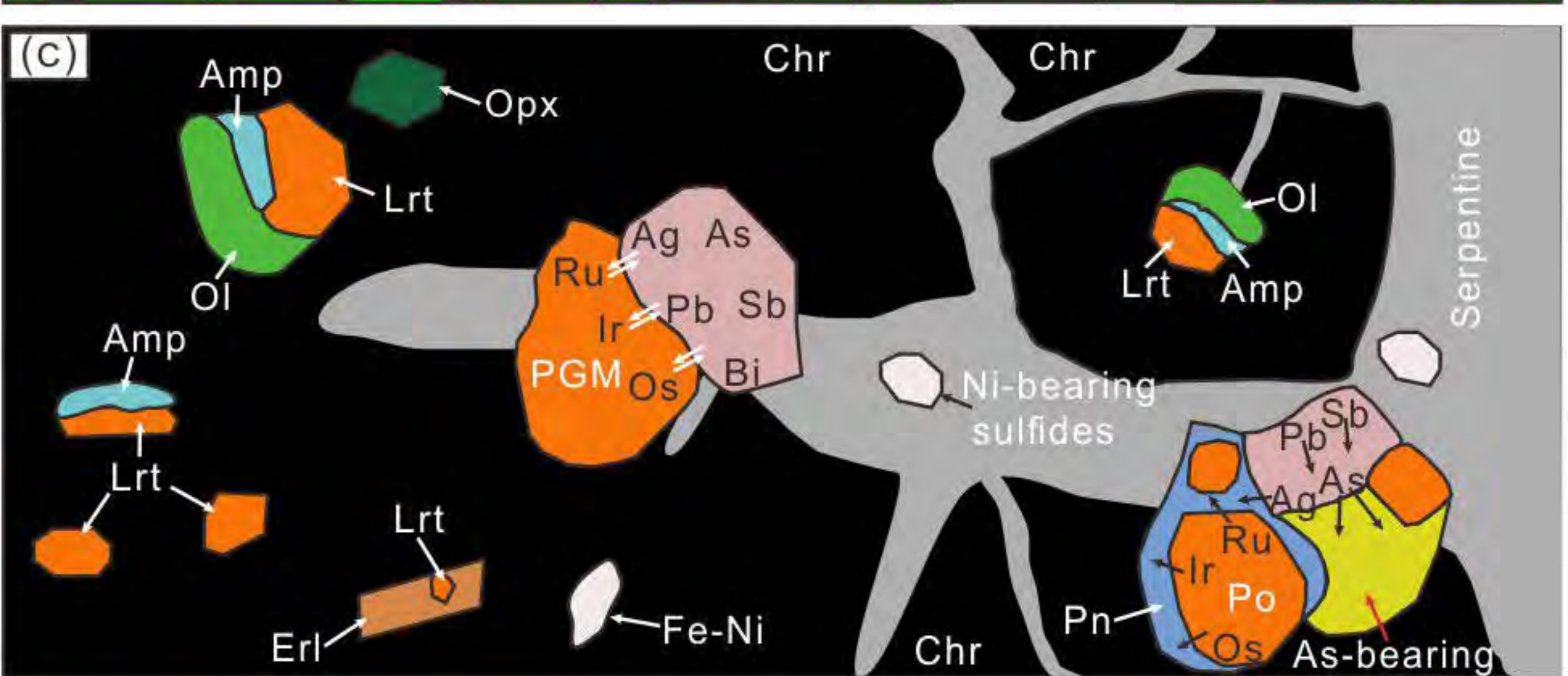
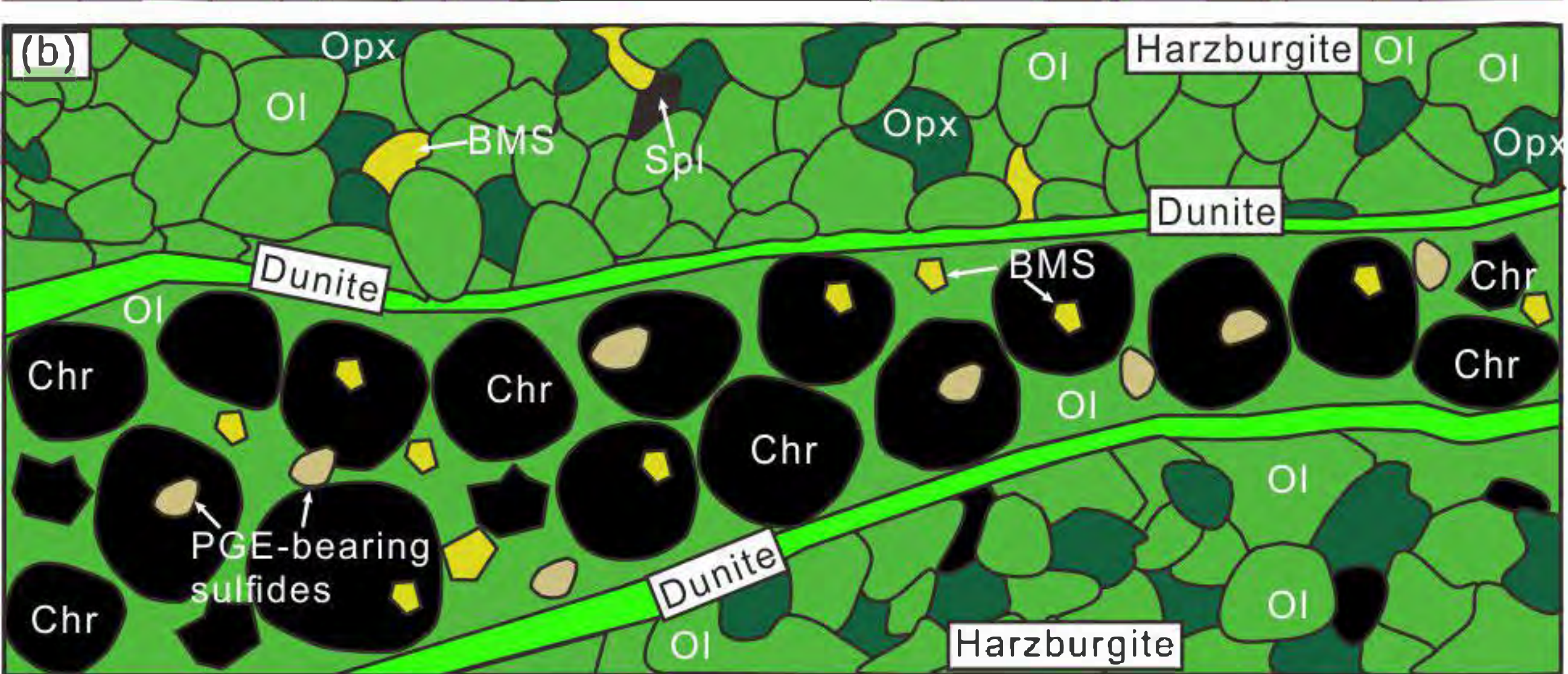
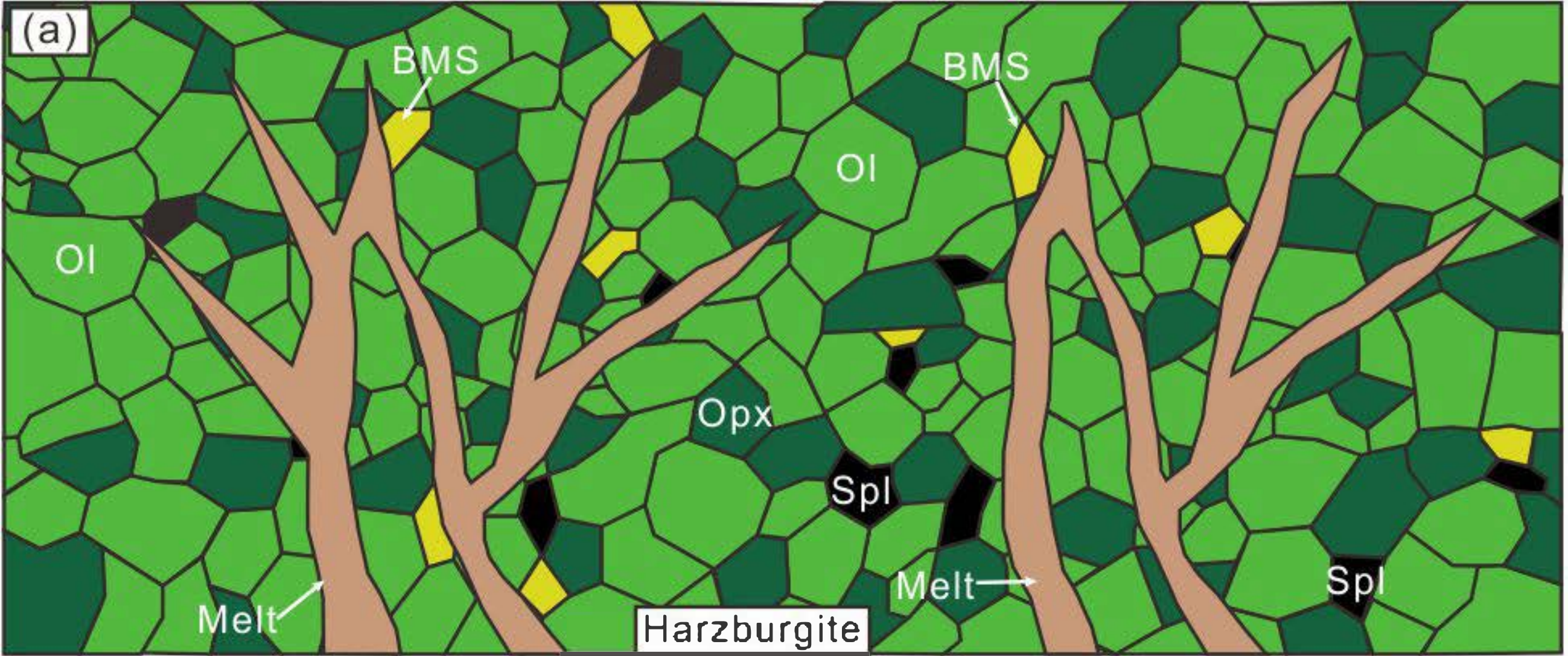


Figure 11